HEAT TRANSFER AND FLOW IN PACKED BEDS WITH NUCLEAR MAGNETIC RESONANCE MICROSCOPY AND COMPUTATIONAL FLUID DYNAMICS

by

Dinal Perera

A thesis submitted in partial fulfillment
of the requirements for the degree

of

Master of Science

in

Mechanical Engineering

MONTANA STATE UNIVERSITY
Bozeman, Montana

November 2017

DEDICATION

This thesis is dedicated to my Father, Mother and Brothers who have supported me throughout my education here at Montana State University.

ACKNOWLEDGEMENTS

Thank you to my committee members, Dr. Ryan Anderson, Dr. Sarah Codd, Dr. Joe Seymour, and Dr. Erick Johnson who have greatly helped me during the entirety of my master's program. Special thanks to Dr. James Maneval and Matt Skuntz who was instrumental in the experimental work. I would also like to extend my gratitude to the graduate students in the NMR lab and the Anderson lab for their support with this process. In addition, I would like to thank Pol Llovet for providing access to the Hyalite Cluster for faster processing of numerical models.

This material is based upon work supported by the National Science Foundation under Grant Number 1511045. Any opinions, findings, and conclusions or recommendations expressed in this material are those of the authors and do not necessarily reflect the views of the National Science Foundation.

TABLE OF CONTENTS

TABLE OF CONTENTS CONTINUED

LIST OF TABLES

Table Page

LIST OF FIGURES

Figure Page

LIST OF FIGURES CONTINUED

Figure Page

LIST OF FIGURES CONTINUED

Figure Page

ABSTRACT

Fluid flow and heat transfer characteristics in packed beds are studied extensively due to its importance in different fields. The macroscopic and continuum approaches used for analysis require a degree of empiricism and theoretical assumptions. Pore-scale models drive out the need for empiricism and theoretical assumptions but cannot be validated due the lack of accurate pore-scale experimental methods. This thesis presents a novel method that utilizes Nuclear Magnetic Resonance (NMR) techniques to map the pore scale melt fraction and velocities within packed beds, non-invasively.

An initial experiment was conducted where heated Nitrogen was flowed through a packed bed filled with PCMs. The increasing signal intensities due to the melting of these PCMs were captured using a ^{1}H tuned coil. Another experiment was conducted where heated Fluorinert was flowed through a packed bed filled with PCMs. The melt front of the PCMs and the velocity of the Fluorinert was imaged using a $^{1}H/^{19}F$ dual tuned coil. Discrete Element Modelling (DEM) was used for the generation of randomly packed beds that mimic the experimental packed beds. These numerical packed beds were modelled under the same inlet conditions as in experimental work to yield models that showed similarities to the processes seen in experimental results.

Numerical work analyzed the effects of particle size and geometry on flow, heat transfer and pore structure. Three models were developed: a packed bed of monodisperse spheres, a bed of spherical particles with a Gaussian distribution in diameters and a bed of non-spherical particles with a Gaussian distribution in diameters. It was concluded that the beds of spherical and non-spherical particles with a Gaussian distribution in diameters yielded the best complementary results to the experimental work. These numerical models and the experimental work yielded maximum velocities in the range of 6 mm/s to 8 mm/s, while showing similar attributes such as intra-particle melt gradients, preferential flow pathways and channeling effect. Experimental work shows a melt front of 60 mm in 41 minutes while models yielded a melt front of 18 mm in the same time.

1 INTRODUCTION

A porous medium is a material that consists of a solid matrix and interconnected voids that allow for flow of fluids. Porous media as seen in nature include rock beds, beach sand, sandstone, limestone and the human lung [1]. Cements, ceramics, foams, filters and membranes are considered to be man-made porous media. Since it became known that this medium can be exploited for improving filtration, waste disposal and other various industrial applications, it has been studied extensively by scientists for many years. In this thesis, the porous medium type, packed bed columns will be studied. A packed bed is a hollow vessel that is filled with packing material such as pieces of metals, ceramics, salt hydrates or catalyst beads. This packing material (solid matrix) forms interconnected voids within them when filled in a vessel, forming a porous medium that allows for fluid flow. Packed beds are used in a variety of industries ranging from the pharmaceutical industry to the energy industry. In the pharmaceutical industry, for example, fixed bed reactors or catalytic reactors are used to improve efficiencies of chemical reactions thereby improving production of pharmaceutical products [2]. In this case, catalytic pellets are the packing material or the solid matrix that forms voids for the flow of reactants. In addition, some reactors require a transfer of thermal energy to or from the solid matrix in order to activate or deactivate the catalyst [3]. Another application of growing interest is packed beds for energy storage in concentrated solar thermal power plants. As seen in Figure 1, all thermal energy is concentrated toward a center tower. A Heat Transfer Fluid (HTF) such as Molten salt is flowed through this tower, which heats the molten salt up to 1000 °C [4]. This hot HTF is then passed through a latent heat storage tank system filled with phase change materials (PCMs). The energy from the hot HTF is then transferred into the PCMs that store this thermal energy (Charging). This stored energy is then extracted by flowing a cooler HTF through the PCMs, which in turn transfers its thermal energy back into the HTF (discharging) which can then be converted into electrical energy through existing processes. PCMs are materials that undergo a change in phase from solid to liquid when heated and from liquid to solid when cooled as shown in Figure 1.

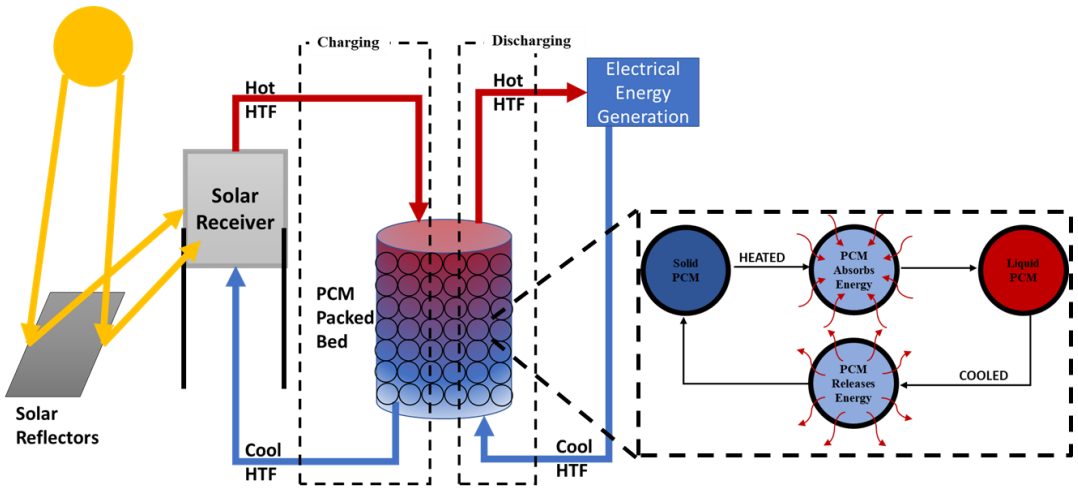

Figure 1: Concentrated Solar Power Plant. A HTF is flowed through a solar receiver which heats the HTF. This heated HTF is flowed through a packed bed which stores the energy as latent heat in PCMs and is known as the charging cycle. A cooler HTF is then flowed through the packed bed which extracts the thermal energy from the PCMs which is known as the discharging cycle. The hot HTF can then be used to produce electrical energy.

Unfortunately, a complete and accurate analysis of packed beds does not exist as no method exists to monitor local velocity and temperature and its coupled effect within a packed bed. Through experimental analysis and/or computational fluid dynamics (CFD), many scientists and mathematicians have developed solutions and models that analyze packed beds. However, existing design equations are often empirical and specific to certain conditions such as porosities and therefore are inaccurate at different conditions. For instance, sensors within a packed bed can measure important parameters such as temperature and flow velocity although this method is known to cause thermal and flow perturbations. Hence, this method does not yield accurate data. One other method is to physically image the flow and thermal energy within a packed bed using different techniques such as CT scans, X-ray tomography, electric tomography, or Infrared imaging [5, 6]. Yet, these methods can be costly and limited. For example, infrared imaging can only yield surface temperatures of packed beds and does not give pore scale information about thermal energy. Electric tomography is known to produce accurate data at the pore scale but can be very costly to run. As mentioned before, packed beds can

be analyzed using CFD but existing models are not verified with experimental data and hence, their validity is in question. There are many reasons for inconsistencies between existing models. One reason is that these models use a continuum approach for ease of modelling and to reduce computational time. However, real life packed beds can vary at the pore scale such as in local porosity. These variations can cause inaccuracies between models and actual beds.

In this thesis, a novel method is presented that can image local temperature and velocity profiles within packed beds, which is then compared to a pore scale CFD model of a packed bed that was randomly packed using the Discrete Element Model (DEM) method. Further details on the DEM method will be provided later in this thesis. Nuclear Magnetic Resonance (NMR) Imaging is used to image a packed bed filled with PCMs as the solid matrix. NMR Imaging of ^{1}H atoms in PCMs yields more signals from the liquid phase than from its solid phase. Therefore, a heated HTF is flowed through this packed bed, which transfers its energy into the PCMs that melt at a certain temperature. The melted liquefied PCMs, in turn, give off more signals than when they were solid, which is picked up in NMR imaging to produce images of higher intensity at locations of melted PCMs. In other words, this method yields a 'light on – light off' effect where the melted PCMs give off a stronger and brighter (light on) signal than those in the solid phase. This phenomenon is exploited to map melt fronts within the bed which can correlate to temperature fronts. The flow of the HTF is then imaged using ^{19}F imaging where existing NMR Imaging methods are used to yield velocity maps within the same bed, allowing for fluid flow and heat transfer within a packed bed to be coupled for analysis. The CFD model, when coupled with heat transfer and fluid flow, allows for pore scale visualization of temperature and velocity, thus providing a numerical complement to the NMR work. A range of relevant heat transfer cases are considered in the experimental and numerical work, including forced convection with nitrogen and also a fluorine-rich fluid through macro PCM packings.

Experimental work utilized packed beds of PCMs that melt at 37 °C with liquid Fluorinert as the HTF to yield melt fronts coupled with velocity maps that showed important attributes such as preferential flow pathways and intra-particle melt gradients.

Furthermore, maximum velocities in the range of 6-8mm/s were obtained. CFD models were then created to complement the experimental conditions to model the flow and heat transfer in a randomly generated packed. In addition, the effects of particle size and geometry on flow, heat transfer and pore structure were explored. Three models were developed, including a bed with monodisperse spheres, a bed of spherical particles with a Gaussian distribution in diameters and a bed of non-spherical particles with a Gaussian distribution in diameters. It was concluded that the latter two models yielded the best complementary results to the experimental work in terms of pore structure and velocities yielded. This was determined by comparing maximum velocities and melt fronts received from the CFD models including the presence of important attributes such as preferential flow particles and intra-particle melt gradients.

This thesis studies these NMR imaging methods, flow loops created and CFD models to complement experimental data. Chapter 2 provides a literature review on the background of fluid flow and heat transfer in packed beds, past efforts at modelling and imaging heat transfer and flow in packed beds including an overview of DEM, and basic NMR theory. Chapter 3 details the experimental conditions used to image flow and heat transfer in packed beds, the numerical methods used to generate randomly packed beds and the numerical conditions used to analyze flow and heat transfer in these beds. Chapter 4 discusses the experimental and numerical results followed by conclusions derived and recommendations for future work.

2 LITERATURE REVIEW

This literature review focuses on existing work on heat transfer and fluid flow in packed beds, including existing CFD modelling efforts and imaging methods. It also provides brief overview of some key CFD methods used in numerical work together with NMR theory utilized in the experimental work.

2.1 Flow in Packed Beds

Porous media can be categorized into consolidated and unconsolidated porous media. Material such as the human lung, rocks and limestone are consolidated porous media because the general domain and the solid matrix are interconnected. Unconsolidated porous media such as beach sand, clay and packed beds have a general domain filled with a solid matrix of loose material. Henry Darcy developed the first equation, now known as Darcy's law, to characterize flow in consolidated porous media [1]. Shown in Equation 1 is the simplest form of Darcy's law which draws a linear relationship between pressure drop and fluid velocity within a porous media, where ∇P represents the pressure drop through the medium, μ represents the dynamic viscosity of the fluid, v represents the velocity of the fluid and K represents the permeability of the bed.

$$\nabla P = -\mu \frac{v}{K} \tag{1}$$

However, since consolidated porous media generally tend to have slower flows through them, Darcy's law is limited to laminar flow. Unconsolidated porous media such as packed beds can have faster turbulent flows and therefore a packed bed Reynolds number is needed to categorize between laminar and turbulent flows. This Reynolds number describes the flow regime in a packed bed as shown in Equation 2, where D_p represents the particle diameter, v represents the superficial velocity of the fluid, and ϕ represents the porosity of the bed. However, over the years there has been much debate on the Reynolds number scale that classify between laminar and turbulent flow.

Generally, it has been accepted that flow in packed beds with Reynolds numbers less than 20 are laminar while numbers greater than 2000 are turbulent [7].

$$Re = \frac{\rho v D_p}{(1-\phi)\mu} \tag{2}$$

Burke-Plummer derived a constant that accounts for pressure drop due to turbulent flow in a packed bed and is the second term on the right-hand side of Equation 3. The Blake-Kozeny equation, being the first term on the right-hand side of Equation 3, is a linear equation that is the reciprocal of the Reynolds number that accounts for pressure drop due to laminar flow. In 1952, Sabri Ergun [7] derived a relation between the Burke-Plummer constant and Blake-Kozeny equation to develop the semi-empirical equation shown below that describes flow in any regime in a packed bed of spherical particles, where *L* is a characteristic length of the bed.

$$\frac{\Delta P}{\rho v^2}\frac{D_p}{L}\frac{\phi^3}{(1-\phi)} = \frac{150}{Re} + 1.75 \tag{3}$$

Unfortunately, pressure drops obtained through the Ergun equation show variation from experimental pressure drops in packed beds of other conditions such as non-spherical particle geometries. This is due to the Ergun constants 150 and 1.75 that were derived empirically and does not account for other influencing parameters. For this reason, the Ergun equation is generalized such as that shown in Equation 4 [8] where the Ergun constants are replaced by α and β. These variables α and β are then derived empirically and theoretically to account for critical parameters such as particle size, particle size distribution and particle geometry. The reader is referred to [9-11] for more information regarding other approaches of modifying the Ergun equation.

$$\frac{\Delta P}{L} = \alpha\frac{(1-\phi)^2}{\phi^3}\frac{\rho\mu v}{d_p^2} + \beta\frac{(1-\phi)}{\phi}\frac{\rho v^2}{d} \tag{4}$$

The Ergun equation and its modification shown above are macroscopic approaches to analyzing flow in packed beds. The flow in packed beds can also be analyzed at the pore scale. This is done by solving at the Navier-Stokes equation, shown in Equation 5, at finite points within the bed where the variable *B* represents the body

force due to gravity. This yields the local pore-scale velocity and pressure of the fluid phase at finite points within the bed [1, 12, 13].

$$\rho_f \left[\frac{\partial v_f}{\partial t} + \nabla \cdot (v_f v_f)\right] = -\nabla P_f + \mu_f \nabla^2 v_f - \rho_f B \qquad (5)$$

However, solving such an equation numerically is challenging and hence, it is simplified using a continuum approach. This is often done using the method of volume averaging to attain an average of flow characteristics over a representative volume. Hsu and Cheng [12-14] uses this method, where they integrated the Navier-Stokes equation with respect to a representative volume to yield Equation 6.

$$\rho_f \left[\frac{\partial}{\partial t}(\phi v_f) + \nabla \cdot \left(\phi v_f v_f\right)\right] = -\nabla(\phi P_f) + \mu_f \nabla^2(\phi v_f) + F \qquad (6)$$

In doing so, the frictional force in the bed is also averaged yielding the variable *F* shown in Equation 6. Similar to variables α and β, closure equations are necessary to determine the average frictional force, *F*. In fact, various literature, such as that published by Whitaker [15], uses the Ergun constants to determine the frictional force, which yields a similar equation to the Ergun equation. The pore-scale approach was used in this thesis as it drives out the need for any empiricism and condition-specific theoretical models due to the absence of variables such as α, β and *F* in the pore-scale Equation 5.

The development of local velocity profiles through various pores in a packed bed is explained by a phenomenon called the channeling effect. Recall that the laminar flow profile through an empty tube follows a parabolic shape with a maximum at the center, governed by the Hagen-Poiseuille law [16]. In a tube filled with solid phases, similar parabolic flow profiles form at local pores bounded between solid phases themselves and the wall [17]. The effect is more clearly shown in Figure 2, where larger maximums are seen in regions of higher local porosities. Therefore, a distribution of velocities is seen due to the variation in local porosity in a bed, which also affects the permeability and inertial coefficients causing a distribution in local heat transfer coefficients.

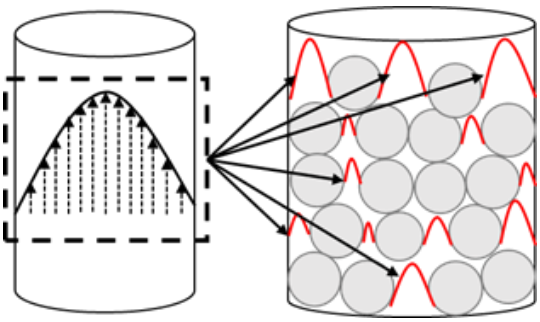

Figure 2: Hagen-Poiseuille type flow profile seen at pores bounded by solid phases themselves and the wall. Higher velocities are seen at larger pores.

The particle size, particle size distribution and particle geometry directly affect the column to particle diameter ratio and the porosity of the bed. The packed beds analyzed in this thesis had column to particle diameter ratios lower than 6:1. Packed beds of such low ratios have seen significant effects on flow and heat transfer due to the inclusion of the wall of a bed [8, 9, 18, 19]. In fact, a significant number of papers published in the field each year study this wall effect. The presence of a wall implies a no slip boundary condition, which induces a shearing stress near the wall and hence, an additional friction on the flow, referred to as the friction effect. On the other hand, the wall forces particles to pack less effectively causing a region of higher porosity by the wall, and hence a higher mass flux consistent with the channeling effect phenomenon, referred to as the porosity effect. Various literature have reported a reduction in pressure due to the porosity effect [20] and an increase in pressure drop due to the friction effect [18]. Recent publications [11] have concluded that these two types of wall effects are Reynolds number dependent and can be explained more clearly by the boundary layer theory. At really low Reynolds numbers such as in the creep flow regime ($Re << 1$), a wall's friction boundary layer is thick enough to dominate the porosity effect causes an increase in pressure drop. At high Reynolds numbers, the wall friction is limited to a thin boundary layer such that the porosity effect dominates and hence, causing a decrease in pressure drop.

The work presented in this thesis is analyzed at higher Reynolds numbers than that of the creep flow regime and so, a few approaches seen in literature that analyze the

porosity effect is discussed. McGreavy et al. [20] demonstrated the velocity distribution in a bed due to the porosity effect by taking measurements using Laser Doppler Anemometry. Figure 3 shows the plot of velocity distributions obtained for a bed of column to particle diameter ratio of 3:1 at four different flowrates, where higher velocities are seen near the walls of the bed due to the porosity effect.

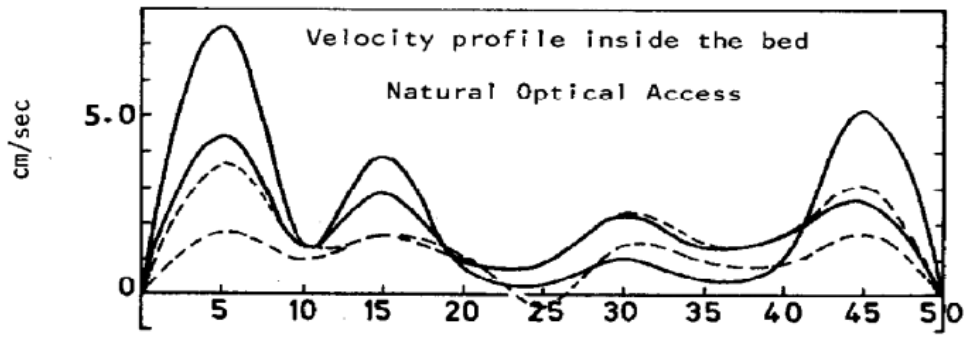

Figure 3: Velocity distribution in column to particle diameter ratio of 3:1 at four different flowrates. Higher velocities are seen near the wall due to the porosity effect [61].

There has been numerous work, both experimentally and theoretically, into developing correlations for α and β of Equation 4 that include this porosity effect. For a detailed review of this work, the reader is referred to [8, 11] where detailed analysis of the correlations together with experimental data is presented.

A frequently used approach to predicting pressure drops in packed beds is the concept of the hydraulic radius. This quantity originally defined in 1922 as the ratio of the wetted volume to wetted surface by Blake [21] is also used in developing the Ergun equation. Mehta and Hawley [18] modified the hydraulic radius to develop a modified friction factor that shows better consistency with experiments results for column to particle diameters ratios as small as 7:1. However, Foumeny et al.[19] showed that this modification shows significant variation from experimental data at smaller ratios. Another approach is the use of a capillary-type model as done by Cheng [8]. In his work, a bed is modelled as a bundle of capillary tubes that are subject to a series of local energy losses represented by sphere drag and a pipe friction term that is summed to calculate the total energy loss. Felice and Gibilaro [9] used the approach of a two-zone flow model that

defines the total mass flux as the sum of the flux in the bulk flow zone and the wall zone. The Ergun equation was used to calculate the flux in the bulk flow zone, which was then used to determine the flux in the wall zone. This approach ties in both the porosity effect and the friction effect at low column to particle diameter ratios.

Particle geometry too has a direct effect on the porosity and the column to particle diameter ratio. Various particle geometries are used in catalytic reactors to increase efficiency. For instance, particles with clover leaf cross-sections offer a greater surface to volume ratio than that of spherical particles. Different geometries pack with different degrees of porosity. It is said roughly that the porosity of a bed increases as the particles deviates from a spherical shape [22]. One major challenge in experimental analysis is the lack of reproducibility of results. This is because the repacking of particles, such as cylinders, causes changes in orientation, which causes variations in pressure drops even in beds of equal porosities. Other particles such as rings or hollow cylinders are known to cause eddies and dead space that affect the flow. It is believed that such particles affect the 'effective' porosity of a bed due to the unavailability of flow through such particles [22], which has been confirmed by Sonntag [23] who reported that only 20% of the interior of such particles are available for flow.

The effect of particle geometry can be characterized by tortuosity of flow developed and the form drag of different shapes. However, due to measurement difficulties, there is a lack of information regarding tortuosity and form drag. Initially, this effect was accounted for by deriving universal constants such as that proposed by MacDonald et al. [10] who proposed universal Ergun constants of 180 and 1.8 for laminar and turbulent flow, respectively. However, models that attempt to derive universal constants have shown significant variation from experimental results. Therefore, it has been agreed upon that universal constants cannot be derived that can capture all effects and hence it is believed that empirical constants are needed for each shape. Investigators such as Nemec and Levec [22] and Hilton et al. [24] simplified this task by categorizing shapes into families depending on the sphericity of the particle. This method seems to be the primary method used today to account for particle geometry effects. The sphericity of a particle as defined by Wadel [25] as the ratio of the surface

area of a sphere which has the same volume as the given particle to the surface area of that particle.

2.2 Heat Transfer in Packed Beds

In 1931, Colburn [26] reported that coefficients of heat transfer for air through a packed bed is about eight times higher than that through an empty tube. He primarily attributed this to the mixing at the pores caused by the introduction of the solid matrix. In the next few years, more than thirty experiments were performed on forced convection through packed columns [1, 27]. The governing equation used for these experiments, shown below, was a continuum approach of analyzing heat transfer in packed beds, where k_e is the effective thermal conductivity of the packed bed.

$$\rho c_p u_m \frac{\partial T}{\partial z} = k_e \left[\frac{\partial^2 T}{\partial r^2} + \frac{1}{r}\frac{\partial T}{\partial r}\right] \tag{7}$$

The heat transfer in packed beds too can be analyzed at the pore-scale using the Energy equation derived from the conservation of energy. This pore scale approach yields a two-equation model that analyzes the energy in the fluid and solid phase separately as shown below [12, 13], where v_f, k_f, and k_s represents the fluid velocity, fluid thermal conductivity and the solid phase thermal conductivity, respectively.

$$(\rho C_p)_f \left[\frac{\partial T_f}{\partial t} + \nabla \cdot \left(v_f T_f\right)\right] = \nabla \cdot (k_f \nabla T_f) \tag{8}$$

$$(\rho C_p)_s \frac{\partial T_s}{\partial t} = \nabla \cdot (k_s T_s) \tag{9}$$

However, solving Equations 8 and 9 numerically can be challenging as well and can be simplified by volume averaging these equations with respect to a representative volume [1, 12, 13]. Equation 10 and 11 represent the volume averaged energy equations for the fluid and solid phase, respectively where h is the heat transfer coefficient of the fluid.

$$\phi(\rho C_p)_f \frac{\partial T_f}{\partial t} + (\rho C_p)_f v_f \cdot \nabla T_f = \phi \nabla \cdot \left(k_f \nabla T_f\right) + h(T_s - T_f) \tag{10}$$

$$(1-\phi)(\rho C)_s \frac{\partial T_s}{\partial t} = (1-\phi)\nabla \cdot (k_s \nabla T_s) + h(T_f - T_s) \qquad (11)$$

This two-equation model is further simplified by assuming local thermal equilibrium between the fluid and solid phase such that T_f=T_s=T. This assumption and adding Equations 10 and 11 yields the single energy Equation 12, which describes the energy of the entire system where k_e is the effective thermal conductivity of the bed [1].

$$(\rho C)_e \frac{\partial T}{\partial t} + (\rho C)_f v \cdot \nabla T = \nabla \cdot (k_e \nabla T) \qquad (12)$$

Equation 12 is similar to Equation 7 such that both these equations analyze heat transfer in a packed bed system using a continuum approach. As seen in both equations, this yields an effective thermal conductivity and effect heat capacity of the system that must be determined using further analysis. There has been a lot of work in determining the effective thermal conductivity of a packed bed and various correlations have been derived using different approaches. The work done in this thesis uses the pore-scale two equation model shown in Equations 8 and 9, which does not require the determination of an effective thermal conductivity or an effective heat capacity. Therefore, only a brief overview of the various correlations derived to determine effective thermal conductivities is presented. The most frequently used model that describes the effective thermal conductivity of a packed bed is the composite layer model [1]. If the heat conduction in the solid and fluid phases occurs in parallel, then the weighted arithmetic mean is used as shown by Equation 13. If the heat conduction takes place in series, such that all the heat flux is passing through both the solid and fluid phases, a weighted harmonic mean is used as shown by Equation 14.

$$k_e = (1-\varepsilon)k_s + \varepsilon k_f \qquad (13)$$

$$\frac{1}{k_e} = \frac{1-\varepsilon}{k_s} + \frac{\varepsilon}{k_f} \qquad (14)$$

These equations provide good estimates if the ratio of thermal conductivity of solid and fluid phases is small. However, for larger ratios, numerous other theoretical approaches have been explored. Nozad et al. [28] defined a system of cubical particles packed in a cubical orientation where the particle-particle contact is modelled as a bridge between neighboring particles. Zehner and Schlunder [29] considered an eighth of a

cylinder with fluid filled between an inner and outer cylinder under the assumption of point contact between the fluid and solid phases. This model has been proven to result in an under-prediction due to the point contact assumption and therefore, Hsu et al. [30] took into consideration finite area contacts between spheres and modified the Zehner and Schlunder model to obtain an equation that has better agreement with experimental data. In addition, numerous experimental approaches have also been used to determine effective thermal conductivities of packed beds. Ofuchi and Kunii [31, 32] used a setup where a steam jacket heated a packed bed and a marble plate of known thermal conductivity. The heat flux in the system was calculated by using the known thermal conductivity and temperatures measured by thermocouples placed at the marble plate. This calculated heat flux and thermocouples placed in the packed bed were then used to evaluate the thermal conductivity of the packed bed.

The previous work described here that determine the effective thermal conductivities and flow effects due to particle size, particle size distribution and particle geometry are limited to various bed conditions and cause significant variations in results when used to analyze beds outside of these conditions. The experimental and computational methods described in this thesis analyze flow and heat transfer in beds of various particle sizes, size distributions and geometries at the pore-scale, avoiding the need for effective thermal conductivities and flow correlations seen in literature.

2.3 Computational Fluid Dynamics (CFD)

This section provides a basic overview of the DEM method and how this method and other approaches have been used in literature to model flow and heat transfer in packed beds.

2.3.1 Discrete Element Model (DEM) method.

P. A. Cundall [33] developed the first DEM method in 1979 to analyze granular physics. Methods such as finite element modelling cannot be used to accurately analyze particle physics. The increase in particle interaction between each other and the domain

has inspired researchers to explore the DEM method for its use in different applications. For this thesis, the DEM method is utilized to generate randomly packed beds. Particles are injected from the top surface of a cylindrical domain at a specified speed and particle flowrate to generate a randomly packed bed using DEM. The DEM method cycles through a series of calculations at each time step with the assumption that at each time step, a particle is only affected by the particles nearest or in contact with it and that other particles away from this particle will not have any effect. With this assumption in mind, the motion of discrete elements or particles can be described using Newton's second law and the force-displacement law. When two particles collide, the volume overlap between the particles is calculated. Assume at time $t=t_0$, two particles are barely in contact, while at time $t_1=t_0+dt$, they are in contact such that they have an overlap. This overlap is calculated by Equation 15, where Δn is the overlap and v being the velocity of a particle at contact. This overlap is then used in the Force-Displacement Law to calculate the resultant force as shown in Equation 16 where k_n is the normal stiffness that depends on the material defined for the particle. This force is then used to calculate the acceleration from Newton's second law and in turn the velocity of the particle.

$$\Delta n = v\Delta t \tag{15}$$

$$\Delta F = k_n \Delta n \tag{16}$$

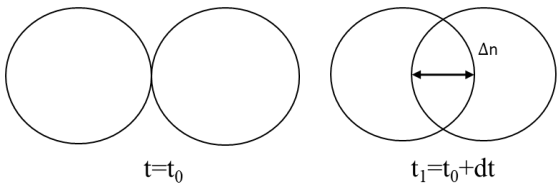

Figure 4: At time $t=t_0$, the particles are barely in contact. At time $t=t_1$, they are in contact such that there is an overlap of Δn.

In a complex system such as that of this thesis, there are multiple particle interactions at a time step. In this case, the resultant forces are used to yield a vector of velocities as shown in Figure 5. Furthermore, to achieve particle equilibrium or in other words to allow particles to settle, a damping function is needed to damp the forces. This

damping is described by particle material properties and other coefficients such as restitution coefficients, static friction coefficients and various contact model constants for particles. For a more detailed description of the DEM method, the reader is referred to [33].

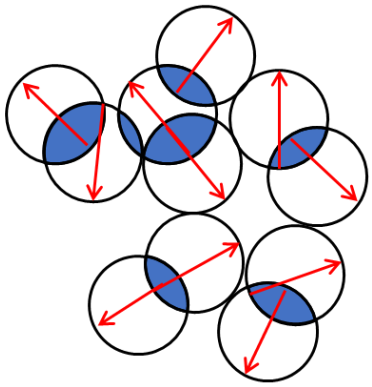

Figure 5: Multiple particle interactions in a DEM simulation. Arrows indicates particle velocity vectors, and the shaded areas represent the particle overlap due to elastic deformation that causes forces.

2.3.2 CFD Analysis Efforts of Flow and Heat Transfer in Packed Beds

Existing CFD models that analyze porous media are either continuum based, pore scale or pore-network (PN) models. The pore-network model has the fundamental limitation of not being able to analyze heat transfer processes within the solid matrix. Therefore, this method is not used in this thesis and will not be discussed here. For further information regarding this method, the reader is referred to [34, 35]. The continuum based models use continuum formulations and coarse grid meshing to analyze packed beds [36]. This type of approach has the advantage of affordable computing costs with minimal computational time. However, this cannot yield pore scale solutions that can characterize local heat transfer processes within pores and particles of the bed. This is because of the coarse-grid mesh whose cells are larger than the average size of the pore.

Pore-scale models, the method used in this thesis, are based on very fine discretization of the general domain that is smaller than the pore size. For these models, existing correlations are unnecessary as equations such as the N-S equations can be

applied at each cell using existing techniques such as the Lattice-Boltzmann method [37] or the Finite Volume method, which is the method used in this thesis. In addition, this approach does not require the use of theoretical assumptions and key influencing parameters can be analyzed. However, this method is limited by its heavy computational cost. Since the fine mesh is smaller than the size of particles, a regular packed bed would require many more nodes than that of the continuum based models. This drives up the computational cost and frequently limits the analysis to a small number of particles. Due to this limiting factor, studies should be strategically defined in order to get the most data without limiting the experimental parameters and realities.

M.T. Dalman et al. [38] developed one of the first pore scale models. In the interest of keeping low computational demands, they analyzed fluid flow and heat transfer through a cylindrical tube filled with two spheres. Finite differencing of the Navier-Stokes equations was used to analyze flow in this two-sphere system. Characteristics of transport were determined for various sphere sizes and sphere separations. They reported an increase in eddies as the sphere separation is reduced or the Reynolds number of the flow is increased. Consequently, the heat transfer through the fluid is affected in that heat is dispersed away from such regions causing a temperature gradient in the system.

Nijemeisland and Dixon [39] used a pore-scale model to analyze the relationship between the local flow field and local heat flux in a packed bed that was generated by precisely placing spheres at pre-determined locations. To reduce computational demands, they limit their study to a column to particle diameter ratio of 4:1 and to a bed height of 6 particle diameters. Using this method, maps of local wall heat flux were obtained giving detailed information about heat transfer properties.

Generating a randomly packed bed is important before analysis can be done as it ensures that the model is valid for any randomly packed bed. Thompson et al. [40] discussed different methods of generating a packed bed to be used for CFD analysis. One commonly used algorithm is the drop and roll type algorithm proposed by Visscher et al [41]. This algorithm results in a bead pack being built sphere by sphere starting from the base, which allows for the study of different media against a range of pack geometries

ensuring information obtained is not specific to one system. In this thesis, the DEM method is used to generate a randomly packed bed similar to the work done in [42]. The primary advantage of using the DEM method in analyzing packed beds is its ability to analyze the motion and resulting forces between individual particles. Literature shows heavy use of the DEM method in analyzing fluidized beds, where the particles are fluidized by the injecting fluid. T. Kawaguchi et al. [43] successfully modelled a fluidized bed with DEM such that they were able to observe the motion of individual particles due to the fluid phase. Further DEM work on fluidized beds has been done by Tsuji et al. [44] and Tanaka et al. [45] who use DEM to model fluid flow through fluidized beds and reported that their results agreed well with experimental data. Further work with DEM are done by Bai et al. [46] and Ookawara et al. [47] to analyze packed beds. It must be noted that the DEM method increases computational demand significantly. Since only fixed beds are analyzed in this thesis, the DEM method was only used to generate a randomly packed bed and was not used in the analysis of flow and heat transfer to save on computational costs.

2.4 Experimental Analysis Efforts of Flow and Heat Transfer in Packed Beds

A macroscopic approach of experimentally analyzing packed beds is the use of pressure sensors to yield pressure drops for packed beds at various conditions. This method was used to derive the Ergun equation and has been used in deriving modifications to the Ergun equation [7, 10, 48]. Many scientists also place thermocouples to measure local temperatures within packed beds [49]. Since this thesis studies pore scale numerical analysis, experimental methods that non-invasively image flow and heat transfer in packed beds will be discussed. The results from different imaging techniques can then be used to validate pore scale numerical models.

One prevalent technique is using X-ray/CT imaging. While these methods can produce relatively accurate images of a porous medium, they have their disadvantages, of which low resolution is a common aspect [6]. Wildenschild et al. [5] provided a comprehensive methodology and analysis of X-ray imaging of porous media. Getting

strong signal to noise ratios have proven to be a challenge with this technique although it must be noted that noise is a ubiquitous feature in any imaging technique. Another imaging technique is Infrared Imaging which has many sources of noise such as detector noise, electronics noise and noise from the external environment. Furthermore, Infrared Imaging produces great results for wall heat transfer but fails in imaging a comprehensive bed.

Nuclear Magnetic Resonance (NMR) Imaging, the method used in this thesis, is an imaging technique that has seen many efforts in analyzing porous media. Nesbitt et al. [50] reported that NMR Imaging can provide an insight into the nature of flow distribution in a porous medium. They further explained that this technique not only yielded qualitative solutions but also accurate quantitative solutions such as flowrates. NMR Imaging can provide high resolution images and is limited by the sensitivity of the fluid to the NMR probe. They concluded that this technique has potential to study catalytic reactors, oil/gas reservoirs and other industrial systems that use packed beds.

A.J. Sederman et al. [51] used NMR to image water flow through a glass bead packed bed. In their experiment, they considered the effects of various regions such as outlet and inlet effects. The data received allowed for a detailed picture of the flow patterns in a packed bed. The structural data of the bed was used to generate a three-dimensional image of the flow. Furthermore, significant distributions in local velocities were observed within the bed with data to support higher velocities near the walls, indicative of preferential flow pathways along the wall. Seymour and Callaghan [52] provided a generalized approach to NMR analysis of flow in packed beds. They used NMR techniques to yield velocities and dispersion data in porous media. Their results show that this technique can be used to yield accurate information of transport phenomena in the spatial and temporal domains, which can then be used to validate CFD models. Yang et al. [53] used NMR Imaging to obtain high resolution three dimensional images of the structure of a packed bed to yield a high resolution three dimensional pore structure. This structure was imported into a CFD application for modelling to yield similar velocity patterns to the NMR images, setting a benchmark for pore-scale validation of CFD models and NMR images.

NMR imaging also has potential for temperature distribution measurements. The sensitivity of temperature on NMR measurements was first shown by Bloembergen et al. in 1948 [54]. This sensitivity can be exploited to non-invasively measure temperature. However, the first methods of two-dimensional NMR imaging of temperature were not explored until 1983 when Parker [55] reported that temperature changes in blood and water samples could be monitored. Parker exploited the sensitivity of T_1 relaxation, a phenomenon discussed later in this thesis, due to temperature and discussed how this could be used to map temperature distributions in human tissue. However, he discussed that there is a tradeoff between spatial resolution and accuracy of temperature measurements and concluded that more work had to be done to more accurately measure temperature spatially. A few other thermometry methods using NMR has been proposed, which are based on phenomena such as molecular diffusion, Proton Resonance Frequency and Temperature sensitive contrast agents. For more information regarding these methods the reader is referred to [56]. Jarenwattananon et al. [57] observed thermal maps in catalyst-packed bed reactors by exploiting the inverse relationship of NMR linewidths and temperature in a weak magnetic field gradient. More specifically, at higher temperatures, gas molecules move faster. This molecular motion is observed in a weak magnetic field gradient by averaging the effects of dephasing to produce narrower linewidths at higher temperatures, which can then be used to map hot and cold spots in a reactor.

The imaging efforts described above fail to couple flow and heat transfer in packed beds. As described previously, flow characteristics greatly impact the heat transfer processes in packed beds. The novel methods presented in this thesis uses NMR imaging to couple velocity maps and melt fronts at the pore scale which is then used to inform CFD models that couple velocity maps and melt fronts.

2.5 NMR Theory

In this thesis, packed beds of encapsulated PCMs were imaged using Nuclear Magnetic Resonance (NMR) technology. The following sections provide a brief overview of NMR theory as described in [58] and its use in methods used for imaging of ^{1}H protons and velocity imaging of ^{19}F protons are discussed.

2.5.1 Nuclear Magnetic Resonance (NMR)

Hydrogen contain nuclei that have an intrinsic spin caused by its angular moment, which imparts a magnetic moment. In an applied magnetic field, the spins align parallel or anti parallel to the field associated with two energy levels. The difference in population in energy levels leads to a spin excess as seen in Figure 6, which causes a net magnetization along B_0 in the longitudinal plane.

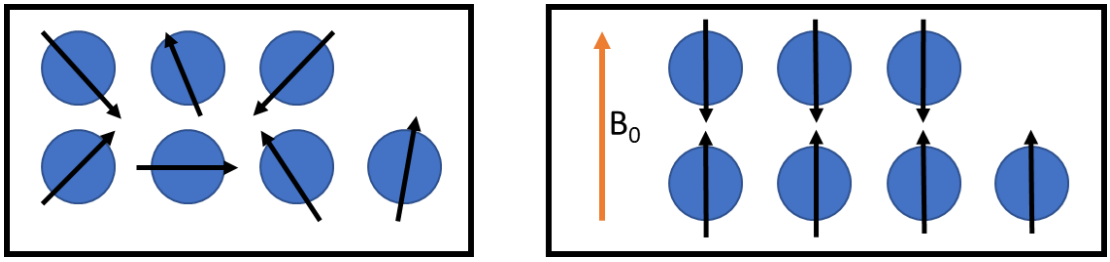

Figure 6: When a magnetic field (B_0) field is applied to a spin system, the spins align parallel or anti-parallel to the direction of the applied field. In this case, there is an excess of spins parallel to the direction of applied field in the lower energy state, in turn, yielding a magnetization vector parallel to the B_0 field.

Even under the applied magnetic field B_0, the nuclei still precess at a frequency called the Larmor frequency that is defined by Equation 17 where γ is the gyromagnetic ratio and B_o is the strength of the applied magnetic field.

$$\omega = \gamma B_0 \tag{17}$$

A radio-frequency (RF) coil is used to induce a magnetic field that oscillates at the Larmor frequency of the specimen, which causes resonance in the system. This RF pulse is transmitted long enough to tip the spin direction from the longitudinal plane to

the transverse plane. When the pulse is removed, the spins remain precessing in the transverse plane. However, with time, the spins start to de-phase in the transverse plane. Transverse magnetization induces a current in the same RF coil yielding what is known as the free induction decay (FID).

Inhomogeneities in the B_0 field cause spins to lose phase in the transverse plane and results in a decaying FID that can that can be refocused as a spin echo. In the NMR community, this decay in signal is known as T_2* decay. A Fourier Transform of the FID provides a spectrum with a linewidth determined by the B_0 inhomogeneity.

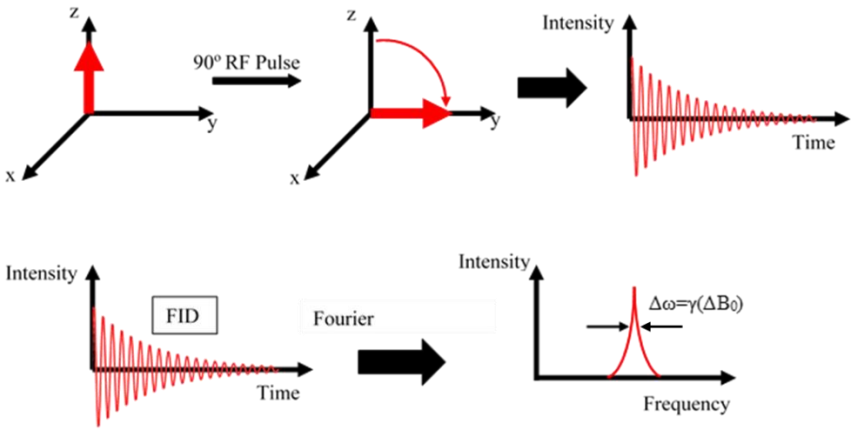

Figure 7: The red arrow shows the magnetization vector along the longitudinal frame. This vector is tipped into the transverse plane using a 90° RF pulse. Once the pulse is removed, the relaxation of the vector back to the longitudinal frame results in a Free Induction Decay (FID) that can be Fourier transformed to attain a spectrum of frequencies associated with the sample.

2.5.2 Laboratory frame vs. Rotating frame

When the process discussed in the previous section is observed from outside the rotating frame, referred to as the laboratory frame, the magnetization vector precesses as it tips to the transverse plane and back. To simplify the mathematics of this process, the analysis is performed from the perspective of the rotating frame. Since in the rotating frame, the x & y axes rotate at the Larmor frequency as well, the magnetization appears to be stationary and can be represented by a single vector as discussed before and as

shown in Figure 7. All equations and theories discussed hereafter will be from the perspective of the rotating frame.

2.5.3 Relaxation

The rate of change of the magnetic moment of a spin bearing nuclei can be represented by Equation 18. This equation results by equating the torque caused by the applied field on the magnetization with the angular momentum of the magnetization vector.

$$\frac{dM}{dt} = \gamma M \times B_0 \tag{18}$$

After the net magnetization is tipped into the transverse plane, the nuclei exchange energy with the surrounding lattice and return back to thermal equilibrium. In doing this, the magnetization returns to the longitudinal plane. This relaxation is called Longitudinal relaxation or T_1 relaxation. The rate of change of this magnetization vector M_z can be represented by Equation 19 whose solution is Equation 20 where T_1 is the time constant for T_1 relaxation.

$$\frac{dM_z}{dt} = -\frac{M_z - M_0}{T_1} \tag{19}$$

$$M_z(t) = M_z(0) + M_0\left(1 - \exp\left(-\frac{t}{T_1}\right)\right) \tag{20}$$

There is another type of relaxation that is useful in NMR known as spin-spin relaxation or T_2 relaxation. This type of relaxation is primarily caused by spins sampling other local magnetic fields from neighboring spins causing a loss in phase coherence of spins. After the initial 90^o excitation, the same oscillating magnetic field can be applied in the transverse plane but for twice the duration resulting in a 180^o pulse that reverses the direction of the spin system. This causes the re-phasing of any signal loss due to T_2* effects, which yields an echo signal. Additional 180° pulses can then be applied to repeatedly re-phase the spins, causing a train echo of echoes. During this process, the amplitude of the subsequent echo signals reduces over time. This decay in signal echo amplitude is known as T_2 relaxation. This pulse sequence, known as the Carr-Purcell-Meiboom-Gill sequence (CPMG), is shown in Figure 8 and is the primary method used to

measure T_2 relaxation. In contrast to T_2*, T_2 relaxation is caused by irreversible energy exchange between spins.

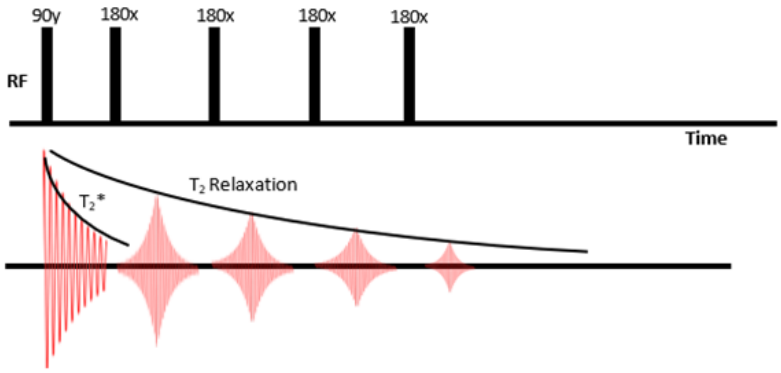

Figure 8: The CPMG sequence used to measure T2 relaxation. The initial 90° pulse tips the magnetization vector onto the transverse plane resulting in an initial FID. Then, repeated 180° pulses causes refocusing of phases yielding a train of echoes. The reduction in signal amplitude of the echoes over time is known as T_2 relaxation

T_2 relaxation is highly dependent on nuclei mobility. In a solid where nuclei are less mobile, T_2 relaxation is faster than in a liquid where the nuclei are highly mobile. This phenomenon is exploited in this thesis where signals are acquired at a fixed time causing an increase in signal strength as the particles transition from solid to liquid. The rate of change of this transverse magnetization can be represented by Equation 21 whose solution is shown is Equation 22 where T_2 is the time constant for T_2 relaxation.

$$\frac{dM_{x,y}}{dt} = -\frac{M_{x,y}}{T_2} \tag{21}$$

$$M_{x.y}(t) = M_{x,y}(0)\exp\left(-\frac{t}{T_2}\right) \tag{22}$$

Equations 18-21 are combined to yield a set of relationships known as the Bloch equations shown below. These equations account for spin relaxation, spin tipping and precession. The rate of change of the magnetization vectors in the x-y plane, M_x and M_y, are functions of the T_2 time constant as M_x and M_y are only affected by the T_2 relaxation. Similarly, the time rate of change of the magnetization vector in the z plane, M_z, is a function of the T_1 time constant as it is only affected by T_1 relaxation. These equations

provide insight regarding the time evolution of magnetization vectors as a function of T_1 and T_2 relaxation. This information can be used to develop pulse sequences, predict signal behavior and provide insight into various NMR phenomena.

$$\frac{dM_x}{dt} = \gamma M_y \left(B_0 - \frac{\omega}{\gamma}\right) - \frac{M_x}{T_2} \tag{23}$$

$$\frac{dM_y}{dt} = \gamma B_1 - \gamma M_x \left(B_0 - \frac{\omega}{\gamma}\right) - \frac{M_y}{T_2} \tag{24}$$

$$\frac{dM_z}{dt} = -\gamma M_y B_1 - \frac{M_z - M_0}{T_1} \tag{25}$$

2.5.4 Nuclear Magnetic Resonance Imaging (NMR Imaging)

The following sections will discuss all theory and methods that yield an image using the NMR basics discussed previously. The basic Spin Echo pulse sequence is discussed which is used to attain a signal from a sample and methods of spatially resolving these signals are discussed together with the method used for velocity imaging.

2.5.5 Spin Echo

A simple spin echo sequence is shown in Figure 9. A 90^o pulse is applied to tip the spins into the transverse plane. The spins in the transverse plane then lose phase coherence as described before. These spin directions are reversed by applying a 180^o pulse in the transverse plane, which refocuses the spin phases. This re-phasing causes an echo signal that can be manipulated to produce an image.

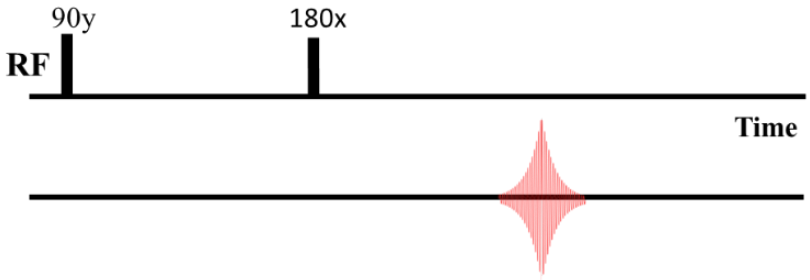

Figure 9: A Spin Echo pulse sequence where an initial 90° pulse tips the magnetization vector onto the transverse plane. A 180^0 pulse reverses the spin direction re-phasing the spins which leads to a spin echo.

2.5.6 Gradients & K-space

In order to attain an image through NMR, a method is necessary to spatially resolve all signals within a sample. In other words, a spatially varying frequency needs to be attained to identify the signals at specific spatial locations. In NMR Imaging, this is achieved by applying a magnetic field gradient across the sample. For simplicity, let us consider a one-dimensional image where a gradient is applied in the z-direction resulting in a gradient described by Equation 26.

$$G = \nabla B_z \tag{26}$$

When this gradient is applied, the spins will precess at local Larmor frequencies depending on their local positions and can be represented by the following equation.

$$\omega_0(z) = \gamma B_0 + z \cdot G \tag{27}$$

In the rotating frame, the spin system yields a transverse magnetization as shown in Equation 29 which calculates the local magnetization density at a certain position z. In other words, it can be said that this equation characterizes the phase evolution over time at different positions.

$$M_+(z,t) = M_+(\mathrm{z},0)\exp(-i\gamma zGt) \tag{28}$$

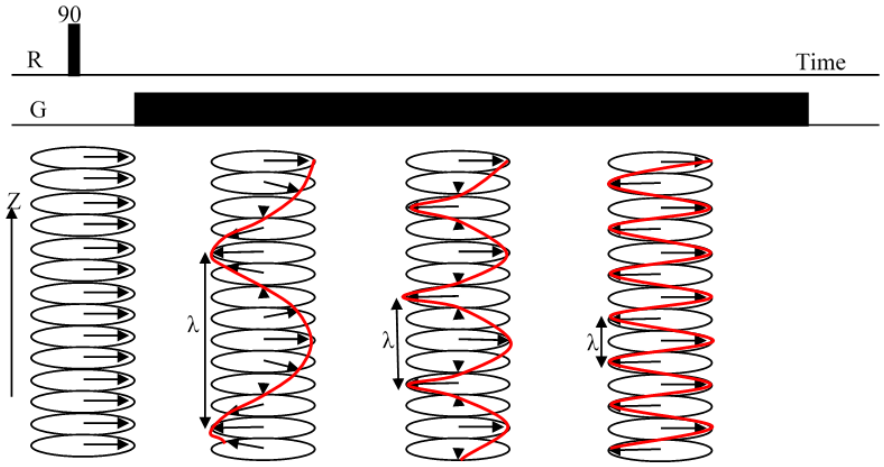

Figure 10: To spatially resolve the signals, a gradient is applied in the z direction. This causes the spin system to precess at location dependent frequencies and causes a winding of helix over time. The wavelength of this helix reduces over time and during the application of this gradient, which can be used to inform on the phase evolution of spins under a specific gradient.

Figure 10 shows the time evolution of the magnetization vectors when a gradient is applied and can be represented by the winding of a helix with wavelength λ. This wavelength reduces with time and can be represented by the following equation:

$$\lambda = \frac{2\pi}{\gamma G t} \tag{29}$$

The wavelength λ provides insight into the phase evolution of spins under the influence of a gradient and is therefore used to represent a vector space known as k-space, which is the reciprocal of λ.

$$k = \frac{\gamma G t}{2\pi} \tag{30}$$

Equation 30 can then be substituted into Equation 28 to yield Equation 31 that describes the phase evolution of the spins under an arbitrary gradient direction at a position z. This k-space needs to be sampled to attain the signals needed to image a sample and can be done so either in time or in gradient magnitude.

$$M_+(z,t) = M_+(z,0)\exp(ikz) \tag{31}$$

The normalized signal attained from the phase evolution of the transverse magnetization in the z direction is defined by the following integral:

$$S_N = \int \frac{M_+(z,t)}{M_+(z,0)}\,dz \tag{32}$$

A new variable known as the normalized spin density represents the number of spins at local positions in the sample. This variable is defined as shown in Equation 34.

$$\rho(z) = \frac{M_+(z,0)}{M_+(0)} \tag{33}$$

Equations 31-33 can then be combined to form equation 34 that describes the normalized signal as a Fourier transform of the spin density. The normalized spin density is then an inverse Fourier transform of the normalized signal. This conjugate pair of normalized signal and spin density is the fundamental relationship that is used in producing a spatially resolved NMR image.

$$S_N(k) = \int \rho(z)\exp(ikz)\,dz \tag{34}$$

$$\rho(z) = 2\pi^{-1} \int S_N(k) \exp(-ikz) dk \qquad (35)$$

Now that the method for attaining the spatial spin density and signal of the sample has been described, methods are needed to sample signals at local positions, which is done by traversing through k-space. As said before, this traversing can be done either in time or gradient magnitude known as frequency encoding or phase encoding, respectively. For the NMR Imaging experiments carried out in this thesis, a combination of frequency and phase encoding was used to traverse through k-space in two dimensions.

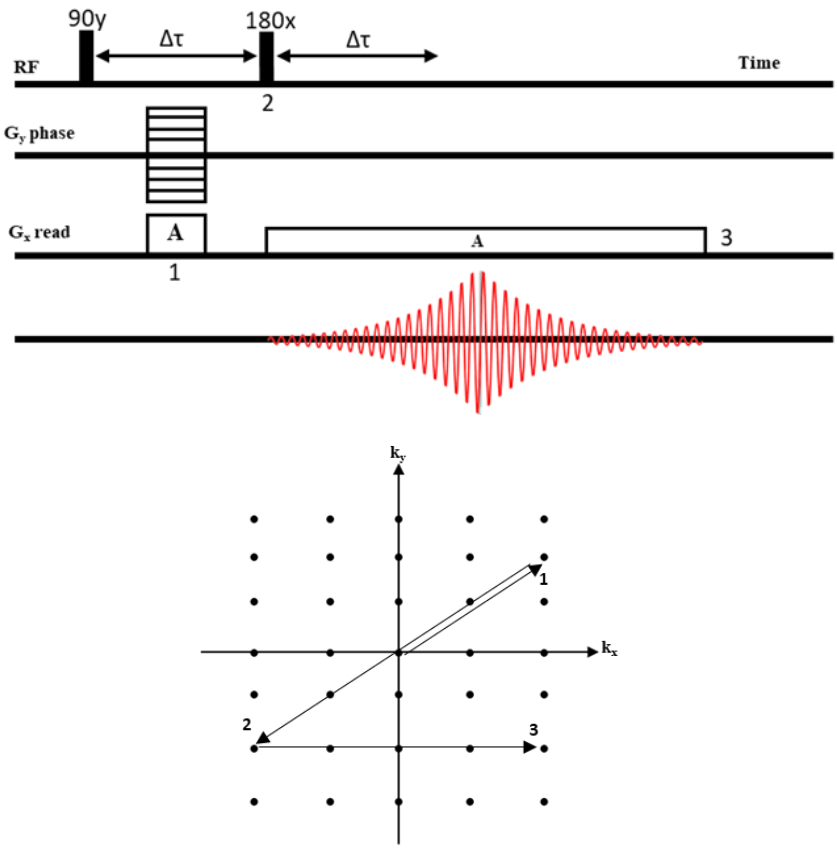

Figure 11: Two-dimensional imaging pulse sequence along with k-space trajectory. After the initial 90^0 pulse, a phase gradient is applied together with a read gradient that causes the traverse labeled (1). Then a 180^0 pulse reverses the spin direction causing the trajectory labeled (2). A readout gradient is applied during which signals are acquired along the trajectory labeled (3). The k_y value sampled is specified by the phase gradient applied at a specific time.

The gradient sequence utilized to traverse through k-space is shown in Figure 11 together with the basic pulse sequence to acquire a spin echo. The sequence starts with a 90^0 RF pulse that tips the spins into the transverse plane. Then, gradient pulses in the x and y direction known as the read and phase direction, respectively, cause a k-space traverse labeled (1) to the edge of k-space. Next, the 180^0 RF pulse inverts all the phases of the spins as described before, and causes the traverse labeled (2). Then, a readout gradient is applied during which acquisition of the spin echo takes place along the traverse labeled (3). Therefore, the acquisition of the signal takes place along the k_x direction at k_y values set by the initial phase gradient. This type of pulse sequence was used in this thesis to image Fluorine (^{19}F) and Hydrogen (^{1}H) atoms in Fluorinert flow and Paraffin melt in PCMs, respectively. For the imaging of Fluorinert velocity, another pulse sequence known as pulse gradient spin echo (PGSE) is combined with the sequence shown in Figure 11 to encode for velocity. A brief overview of the PGSE sequence is provided in the next section.

2.5.7 Pulse Gradient Spin Echo (PGSE)

For the purposes of this overview, consider the velocity encoding in the z direction. After the initial 90^0 pulse is applied, the spins are de-phased by applying a gradient in the z-direction. The spins are then re-focused using an 180^0 pulse as described in the previous sections. Another gradient of the same magnitude is applied after the 180° pulse, in turn, re-phasing the spins. However, if a spin-bearing molecule moves within this time frame, the spin would not re-phase and a residual phase shift would be observed as seen in Figure 12. This residual phase described by Equation 36, can be used to determine the displacement of a spin bearing molecule in the time between the two gradient pulses, Δ. Since Δ is user specified and is known, the velocity of this spin bearing molecule can be calculated. As mentioned before, this pulse sequence is combined with the pulse sequence in Figure 11 to acquire data for a velocity image such as the ones shown in the results section of this thesis. In Equation 36, g is magnitude of the gradient applied and δ is the duration of the gradient.

$$\Delta\varphi = \gamma\delta g(z_1 - z_2) \tag{36}$$

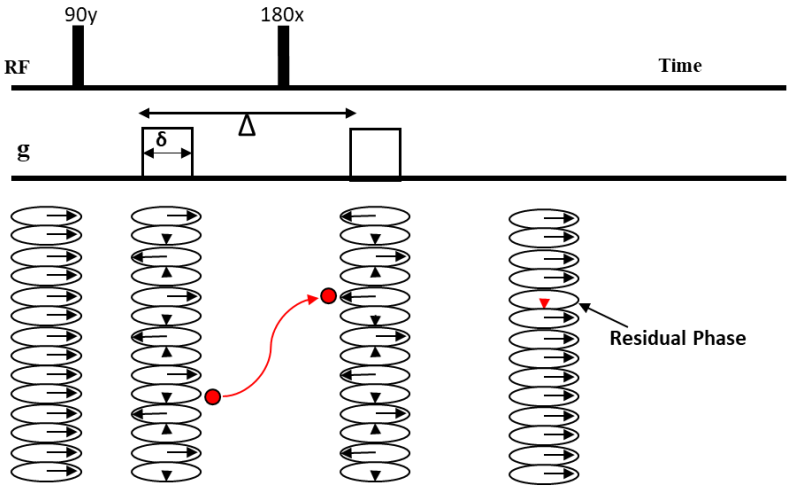

Figure 12: The PGSE sequence - after the initial tip on to the transverse plane, a gradient is applied to de-phase the spins according to their local positions. After a certain time and after the 1800 pulse, a gradient with the same magnitude is applied, to re-phase the spins. If a spin bearing molecule moved during this time, a final residual phase will occur during re-phasing.

In 1965, this effect on magnetization due to flow and diffusion was characterized by Torrey [59] who modified the Bloch equations shown previously. This modified Bloch-Torrey equation is shown in Equation 37 and is used to attain information about velocity. Just like the original Bloch equations, this modified equation provides a great deal of insight into NMR processes including the effect of diffusion and velocity of a sample on the time rate of change of the transverse magnetization.

$$\frac{dM_+}{dt} = -i\gamma \cdot g(t)M_+ - \frac{M_+}{T_2} + D\nabla^2 M_+ - (v \cdot \nabla)M_+ \tag{37}$$

3 EXPERIMENTAL & NUMERICAL SETUP

This section discusses the design of a domain used to create an experimental packed bed together with the stress analysis and testing done to ensure it can handle the necessary pressures. Furthermore, the flow loop setup used for NMR imaging of heated Fluorinert flow through a packed bed is discussed together with the experimental conditions used. Then, information regarding the Numerical conditions, the melting model used, the meshing method and random packed bed generation is discussed.

3.1 Design of Sample Holder

Before a packed bed column is imaged using NMRI, a hollow vessel that can hold packing material was designed and built. The material chosen for the vessel had to be strong enough to sustain under a high pressure while also ensuring that the material does not affect the NMR signals. Polyetheretherketone (PEEK) was chosen as it has a high yield stress of approximately 75 MPa and is proven to not affect NMR signals. In addition, there were other design restrictions that had to be adhered to such as geometry, inlet diameter, length, and pressure rating. The vessel would need to be placed inside a RF coil, which had a cylindrical bore of 25 mm. In addition, the vessel would need to have an appropriate wall thickness that would be able to handle a pressure of at least 100 Bar. This vessel would need to be accessible for repeated packing to form packed beds of various porosities. Therefore, the vessel was built as two halves as shown in Figure 13 where the male half with external threads can be screwed into the female half with internal threads. This makes the vessel accessible for packing with different types of PCMs.

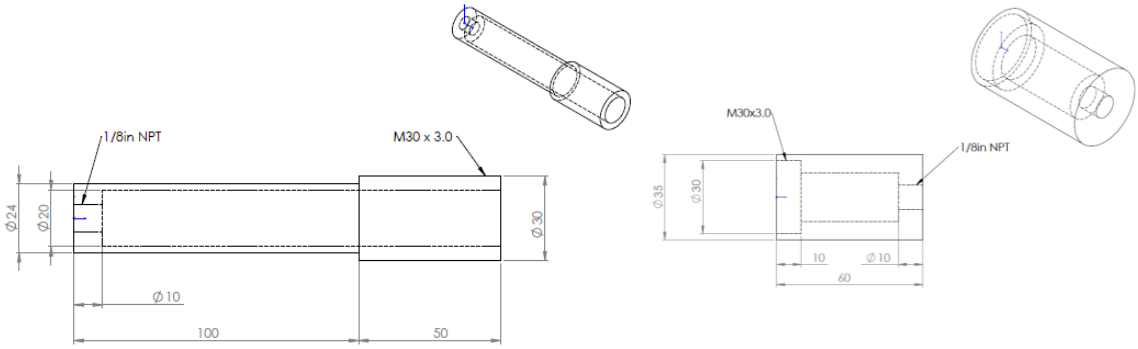

Figure 13: The PEEK sample holder designed and manufactured. As can be seen, the vessel can be screwed off from the center to pack in PCMs.

It was necessary to maximize the inner diameter of the vessel in order to pack the maximum possible amount of PCMs. Since the maximum outer diameter was limited to 25 mm, the wall thickness had to be optimized to ensure the maximum possible inner diameter whilst being able to hold a pressure of 100 Bar. The vessel was treated as a thin walled pressure vessel where the hoop stress is known to be the largest stress and hence the limiting factor. A detailed overview of the calculations used to attain an appropriate inner radius and wall thickness is included in the Appendix. In summary, the hoop stress equation shown in Equation 39 considers the pressure in the system together with the inner radius and wall thickness of the vessel where P_{max} is the maximum pressure and r_o and r_i are outer and inner radius, respectively.

$$(\sigma_h)_{max} = \frac{P_{max} r_i}{r_o - r_i} \tag{38}$$

By setting a safety factor of 1.5, the following equation was solved to yield an inner radius of 10 mm where σ_y is the yield stress of PEEK.

$$1.5 = \frac{\sigma_y}{(\sigma_h)_{max}} \tag{39}$$

This design was then commissioned to 4MRnD Machining for manufacturing. After the vessel was built, it was pressure tested to ensure that it can hold up to 100 Bar without failure. The vessel was tested in a steel container to ensure that it did not cause any injury or damage to surrounding equipment if it did fail. Nitrogen was pumped into the vessel and pressurized gradually starting from 10 Bar. A leak was located initially at the M30x3.0 threads of the vessel, the section designed to be unscrewed for packing. This

leak was fixed by placing an O-ring between the female and male part and thereafter tested until 100 Bar with no indication of failure.

3.2 Flow System used for Heated Nitrogen Flow through a Packed Bed

Figure 14 shows the flow system utilized to transport heated nitrogen into the sample holder filled with PCMs. A Bruker BVT 30000 unit was used to pump nitrogen into a Micro 2.5 Temperature Control Probe. An inline electric coil heater within the probe heated the nitrogen as it flowed through the probe. A thermocouple at the top of the probe, just below the sample, was used with a PID controller to maintain the set temperature of the nitrogen entering the sample.

.

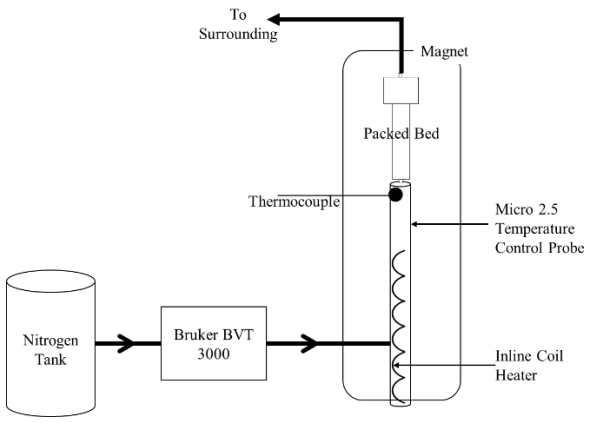

Figure 14: Flow System used for Nitrogen Flow through a packed bed

3.3 Flow Loop used for Heated Fluorinert Flow through a Packed Bed

Figure 15 shows the flow loop utilized to transport heated Fluorinert into a PCM packed bed held within the magnet. A peristaltic pump was used to pump Fluorinert held in a beaker through a heat exchanger, which is shown in further detail in Figure 15b. HPLC tubing was used to transport Fluorinert. A coil of this tubing is placed in a heat bath for heating. In addition, the HPLC tubing was passed through a larger 1/2" tube that circulated heated water between the outlet and return of the heat bath, heating the

Fluorinert while it was transported from the heat bath to the packed bed held in the magnet. 1/2" Armaflex insulation was used to insulate the entire heat exchanger, from the heat bath to the magnet, to minimize heat loss from the system. The HPLC tubing was connected to the packed bed via a 3 mm inlet. This packed bed was then placed inside the magnet, where the outlet of the bed is connected to HPLC tubing that transport the Fluorinert back to the same initial beaker.

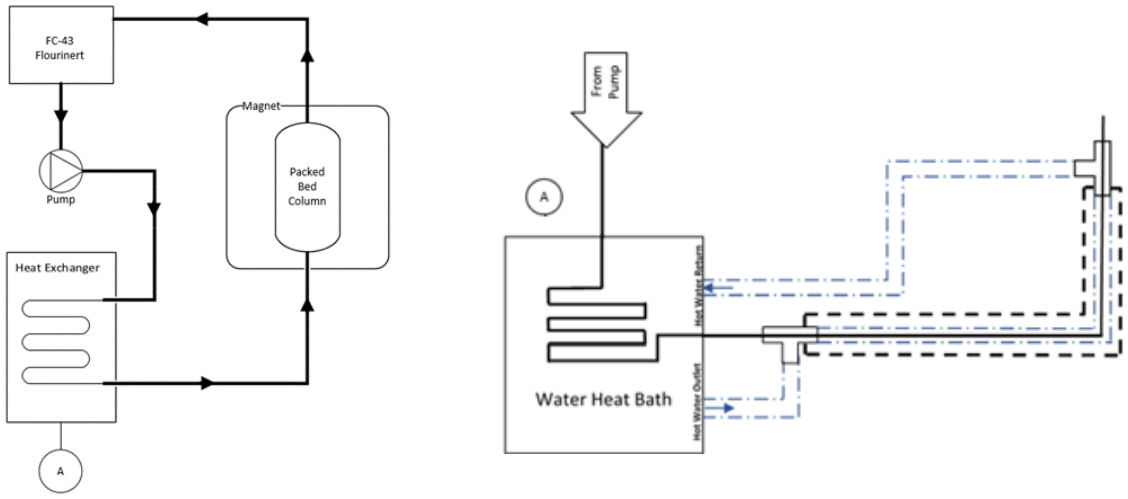

a) **b)**

Figure 15: (a) Macroscopic flow loop built to flow heated Fluorinert through packed beds (b) Detailed schematic of the heat exchanger system used.

When this flow loop was tested, it was also calibrated to find the Fluorinert temperature at the inlet of the packed bed, parallel to the flow. A thermocouple was placed at the end of the tube that connected to the inlet of the bed, and the temperature was recorded until it reached equilibrium. The heat bath temperature was changed to find different inlet temperatures at three different flowrates, which is shown in Figure 16. This scatter of data was fit with linear fit that was used to attain the necessary heat bath temperatures for the desired specific inlet temperature.

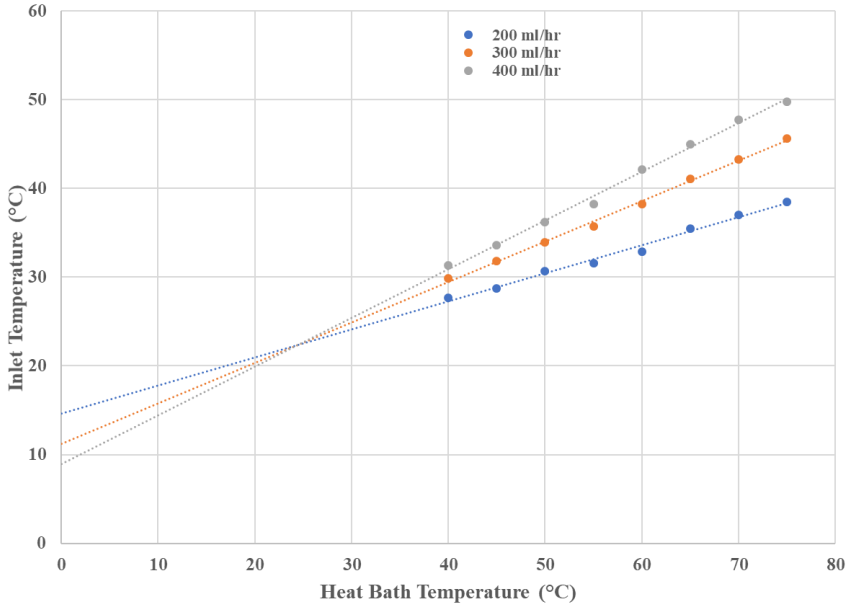

Figure 16: Plot of Inlet Temperature vs. Heat Bath Temperature. The equation from the linear fit was used to calculate the necessary heat bath temperature for a specific inlet temperature.

3.4 Experimental and Numerical Conditions

Two experiments were conducted for NMR imaging. The first experiment involved the flow of heated Nitrogen gas into the PEEK sample holder packed with MacroPCM 37C beads. This allowed hydrogen imaging of the PCMs, allowing for a melt front to be imaged with time. The second experiment consisted of flowing Fluorinert liquid through a 10 mm HPLC column filled with MacroPCM 37C beads. Fluorinert was chosen as it is a fluorine-rich liquid that can be imaged using the available $^{1}H/^{19}F$ dual tuned coil that allows for the imaging of both the melt front of PCMs and the velocity profile of Fluorinert flow. Table 1 shows the inlet conditions used in each experiment. In addition, a 40 mm Field of View (FOV) was used for NMR imaging at the packed bed locations shown in Figure 17.

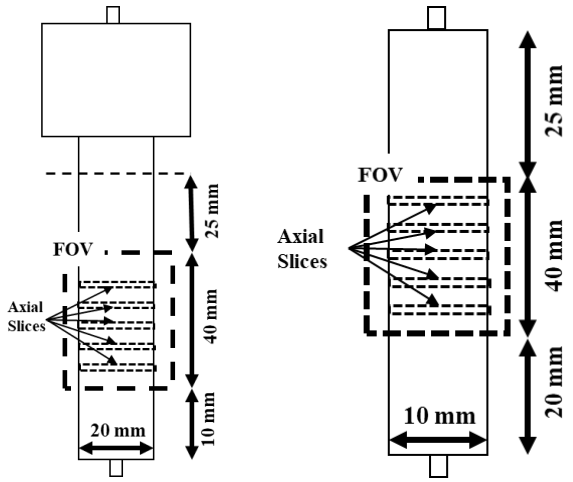

Figure 17: a) Packed bed used in Nitrogen Flow experiment with a total bed height of 75 mm. b) Packed bed used in Fluorinert Flow experiment with a total bed height of 85 mm

For the CFD modelling of the Nitrogen flow experiment, a packed bed was generated in a PEEK domain of similar bed diameter and height to that of the experimental work. The packed bed generated consisted of spherical particles with a Gaussian distribution in diameters. Nitrogen gas was flowed through this bed with an inlet temperature of 45 °C at a mass flow rate of 9.838E-5 kg/s. This is the equivalent mass flow rate for the experimental volumetric flow rate of 270 L/hr if the density of Nitrogen was assumed to be at 1.251 kg/m^3.

For the CFD modelling of the Fluorinert flow, three packed beds were generated in glass domains with similar bed diameter and height to that of the experimental work. Glass material was specified because the HPLC column was made of glass. Three packed beds were generated, which included a bed of monodisperse spheres of 3.77 mm diameters, spherical particles with a Gaussian distribution in diameters, and non-spherical particles with a Gaussian distribution in diameters. Liquid Fluorinert was flowed through these beds with an inlet temperature of 38.5 °C at a mass flow rate of 1.033E-3 kg/s, which is the equivalent mass flow rate for the experimental volumetric flow rate of 200 mL/hr. The properties shown in Table 2 were specified for the Nitrogen gas, liquid Fluorinert, PCMs, PEEK and Glass domains, which were based on literature values [60].

Table 1: Summary of Experimental Conditions and Numerical Conditions. Same inlet conditions were used for both Experimental and Numerical models. Three different packed beds were modelled for numerical analysis.

Inlet Conditions	**Experimental Packed Beds**	**CFD Packed Beds**		
		Monodisperse Spheres	**Gaussian Spherical**	**Gaussian Non-Spherical**
Nitrogen Flow				
270 L/hr 45°C	17mm PEEK Domain filled with Macro PCM37C		**X**	
Fluorinert Flow				
200 mL/hr 38.5 °C	10mm HPLC Column filled with Macro PCM37C	**X**	**X**	**X**

Table 2: Material properties specified in CFD model for Nitrogen gas, Fluorinert liquid, PCMs, Glass and PEEK domains. Nitrogen molecular weight is specified as density changes with temperature.

Property	**Nitrogen**	**Fluorinert**	**PCMs**	**PEEK**	**Glass**
Density (kg/m^3)	1.0738 at Inlet	1860	780	1320	2300
Molecular Weight (kg/kmol)	28.0134				
Specific Heat (J/kg-K)	1040.76	1100	2900	320	795
Thermal Conductivity (W/m-K)	0.0256	0.065	0.82	0.25	1.13
Dynamic Viscosity (Pa-s) (T_{ref} =298.15 K)	1.79E-05	0.0047			
Latent Heat of Fusion (J/g)			200		
Melting Point (°C)			37		

3.5 Packed Bed Generation

An important aspect of the CFD work carried out in this thesis is the random generation of a packed bed to mimic experimental packed beds. Eppinger et al. [42] used the DEM capabilities in Star-CD to form a randomly generated packed bed. A similar method was used to generate packed beds in this thesis. However, in [42], only monodisperse spherical particles are generated whereas in this thesis, spherical particles of varying diameters and non-spherical particles of varying characteristic diameters are generated. The characteristic diameter is defined as the diameter of a sphere of the same volume as the non-spherical particle.

Star CCM+'s DEM capabilities were coupled to form a randomly generated packed bed. One of the domains created was the 10mm diameter borosilicate glass cylinder with a height of 85 mm similar to the bed height used in experimental work with Fluorinert.

The DEM required the setup of a Langrangian phase to represent the geometry of the PCMs. Three packed beds were generated where two beds used a spherical particle geometry and the other used three non-spherical geometries. For each Langrangian phase defined, the interactions of PCMs themselves and the walls were defined. This is a vital step in the DEM process as it defines how the PCMs interact as they come in contact with the domain and with themselves. A no-slip contact model was chosen for interactions, which required the definition of various parameters as shown in

Table 3. The static friction coefficient is used in calculating the tangential forces due to the interactions of PCMs with one another and the domain wall. The Normal Restitution coefficient and Tangential Restitution coefficient are used to determine the kinetic energy lost upon the interaction of PCMs. This in turn determines how quickly PCMs come into a relatively zero velocity after interactions. The values for these terms were defined upon research into literature [42] and modified to ensure a quick settle. The Coefficient of Rolling Resistance, which was left at its default value, determines the rolling friction between contact models.

Table 3: The parameters defined in Star CCM+ for PCM interactions between themselves and Walls. These coefficients are used in calculating the resultant force and the loss of kinetic energy after interaction

PCM-PCM/PCM-Wall	
Static Friction Coefficient	0.61
Normal Restitution Coefficient	0.5
Tangential Restitution Coefficient	0.5
Coefficient of Rolling Resistance	0.001

After the particle domain and particle interactions were defined, the top surface of the cylinder was defined as an injector as shown in Figure 18. A particle flow rate of 200/s was defined together with the particle diameter. The first bed generated consisted of spheres of a constant diameter of 3.77 mm. This constant diameter was the average diameter of PCMs used in experimental work, which was calculated by counting the total number of PCMs and determining the total volume occupied by these PCMs.

A time step of 0.0001s was specified for the simulation. During the simulation, PCMs were injected from the top surface as shown in Figure 18a. Once the bed was filled with PCMs, the injector surface was closed by defining the top surface as a closed wall. The simulation is then run again to allow for the beads to settle such that they converge to a relatively zero velocity. This yields a packed such as the one shown in Figure 18b.

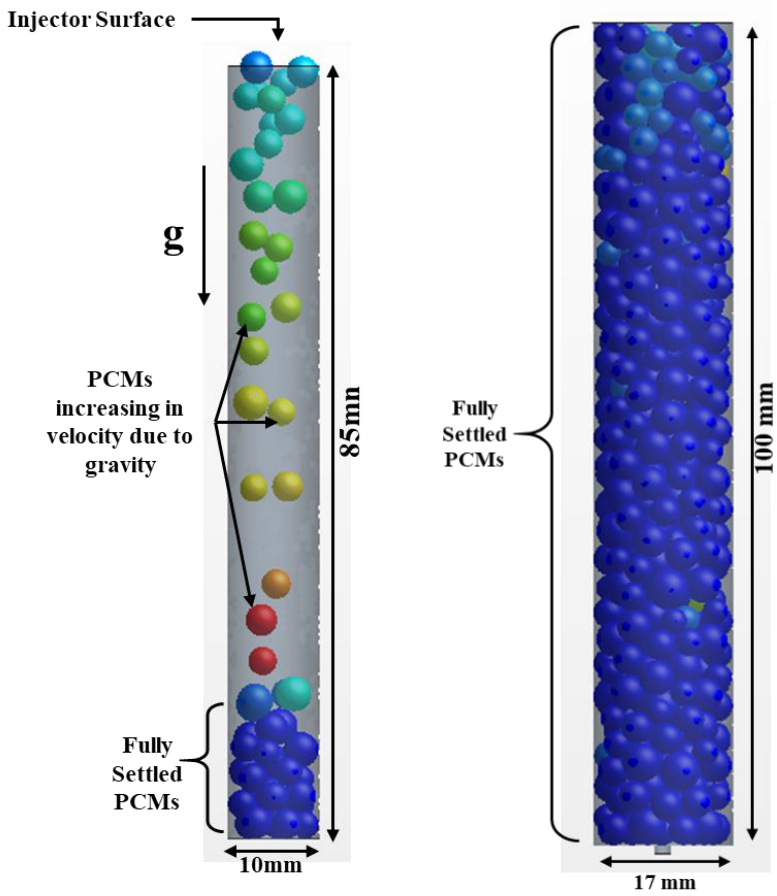

Figure 18: (a) Injection of PCMs with Gaussian distribution in diameters and their interactions. Packed bed used in modelling Fluorinert flow through packed bed. The different colors represent the velocity of PCMs. The blue color showing a relatively zero velocity while the red shows a maximum velocity reached due to gravitational acceleration. b) The fully settled packed bed of PCMs with a Gaussian distribution in diameters used to model nitrogen flow through packed bed.

After a 3.77 mm spherical particle bed was generated, it was deemed that another approach was necessary. The second packed bed generated consisted of spherical particles with a Gaussian distribution in diameters. This method was chosen as it was noticed that the PCM manufacturer specified a diameter in the range of 3mm to 5mm. Therefore, within the injector setup, the particle diameters were defined as a Gaussian distribution in diameters between 3 mm and 5 mm with a mean of 4 mm and a standard

deviation of 1 mm. This yields the Gaussian distribution shown in Figure 19, which was truncated at the minimum and maximum values specified.

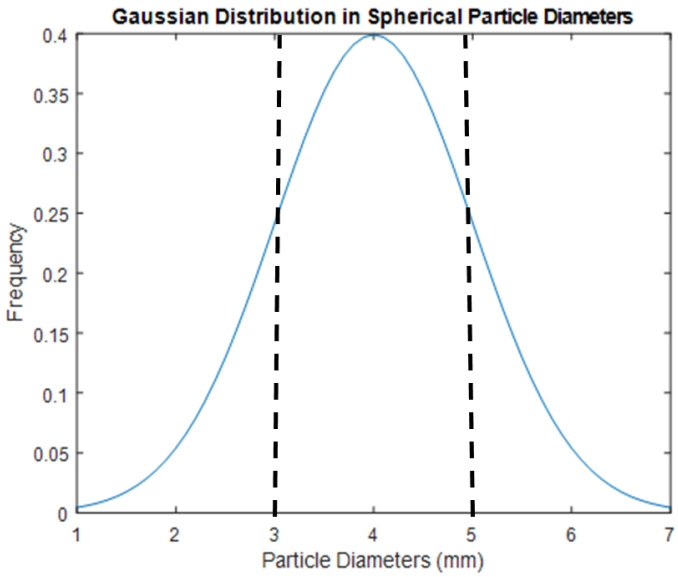

Figure 19: Gaussian distribution in spherical particle diameters used to generate a packed bed. Diameters = 3mm to 5mm, σ=1mm, μ=4mm

Literature has shown that non-spherical particles cause variations in pressure drop when compared with perfectly spherical particles [22, 24]. Since the experimental PCMs were not perfect spheres, another approach was taken to model the non-sphericities of the particles. The experimental PCMs were examined closely and three frequently occurring shapes were drawn and modelled on the CAD module available on Star-CCM+. The CAD models for the three non-spherical shapes drawn are shown in Figure 20a. With this approach, three Langrangian phases were set up that utilized the CAD models by using a composite of spheres so that DEM can still be used to generate a packed bed. Furthermore, these three particles were then injected using three different injectors with the same flow rates and Gaussian distribution in diameters for each shape. Then, using the same injection procedure as described previously, a packed bed was generated as shown in Figure 20b.

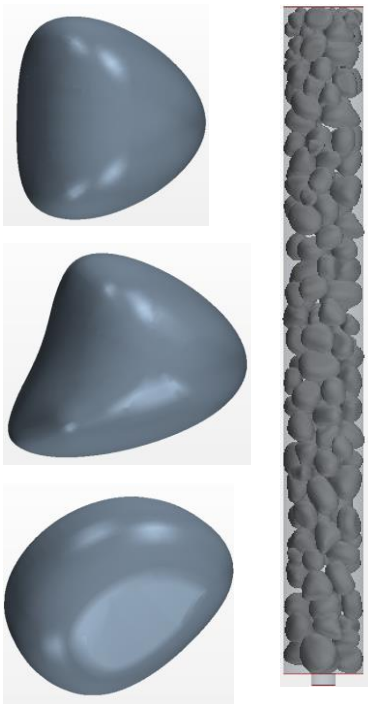

a) **b)**

Figure 20: a) Three non-spherical shapes used to generate the non-spherical packed bed. b) Packed bed generated using non-spherical particles with a Gaussian distribution in diameters

Another domain was created to complement the Nitrogen flow experiment. The packed bed used in this experiment used the sample holder described previously and so a cylindrical domain with a diameter of 17 mm and a height of 100 mm was created for the CFD model. A packed bed was generated for this domain using spherical particles with a Gaussian distribution in diameters, which is shown in Figure 18b.

3.6 Melting and Meshing Models used in CFD

The Melting model used in the CFD work utilized an existing physical model available on Star CCM+ that is applied to individual PCM volumes. This model does not track the liquid-solid interface explicitly. Instead, the model uses an enthalpy formulation to determine the solid phase of a liquid-solid phase. This enthalpy formulation, shown below, calculates the enthalpy of the liquid-solid phase (h_{ls}^{*}) using the sensible enthalpy (h_{ls}) or the specific heat capacity, the solid volume fraction (α_s^{*}) and the latent heat of fusion (h_{fusion}) of the material specified.

$$h_{ls}^{*} = h_{ls} + (1 - \alpha_s^{*}) h_{fusion} \tag{40}$$

A normalized temperature is calculated using the melting temperature ($T_{liquidus}$) and solidification temperature ($T_{solidus}$) as shown in Equation 42, which is then used to calculate the relative solid volume fraction (α_s^{*}) of the volume where 1 and 0 represents a solid and liquid phase, respectively.

$$T^{*} = \frac{T - T_{solidus}}{T_{liquidus} - T_{solidus}} \tag{41}$$

$$\alpha_s^{*} = \begin{cases} 1, & T^{*} < 0 \\ 1 - T^{*}, & 0 < T^{*} < 1 \\ 0, & 1 < T \end{cases} \tag{42}$$

The values shown in Table 3 were specified for the PCM material. The Solidus and the Liquidus temperatures were both set to the melting point of 37 °C. However, if Equation 42 is examined carefully, one would notice that T^{*} would be undefined if both the solidus and liquidus temperatures are the same. Therefore, to eliminate this error, Star-CCM+ automatically applies an interval of 0.002 °C between the two temperatures. This results in a solidus temperature of 36.999 °C and liquidus temperature of 37.001 °C. Meshing is an important aspect in CFD. With the use of the DEM, particles have particle-particle contact and particle-wall contact. These regions often cause meshing issues such as mesh matching and hence, many approaches exist to eliminate this error. Eppinger et al. [42] uses DEM to generate a fixed bed reactor with small tube to particle diameter ratios. Once the bed was generated, the surfaces of the particles were extracted and the DEM method was not used for the modelling of flow. To eliminate meshing issues, they

flattened all points of contact in particle surfaces such that the gaps between surfaces are so small that the velocity is zero at that region.

In the work done in this thesis, techniques were used to mesh the packed bed without the need to flatten contact points. Three primary meshing techniques were used. The surface meshing was done by using Star CCM's Surface Remesher and Automatic Surface Repair techniques while the volume meshing was done using a Polyhedral Mesher. A working surface mesh was necessary to prepare the domain for volume meshing. Two inherent techniques were available, which were the Surface Remesher and the Surface Wrapper. The Surface Remeshing technique was used as it maintains the original features of the domain to provide important information with no loss to the surface detail. Meshing a surface is the dividing of the domain into a grid of elements that can be analyzed individually. Therefore, with this surface meshing technique, the elements are triangulated to produce a detailed mesh, as shown in Figure 21a. The surface meshing is primarily based on the target edge length that is specified and is refined using curvature and surface proximity parameters. Once the Surface Remeshing produces a detailed mesh, the Automatic Surface Repair tool is used to further refine the mesh especially in areas of contact. This tool uses an iterative process to refine the mesh until a sufficient surface quality as shown in Figure 21a is achieved. Once the surface meshing is completed, Polyhedral meshing is used to yield a volume mesh as shown in Figure 21b. This type of meshing works by utilizing arbitrary polyhedral cell shapes shown in Figure 21c to fill the core of the volume as shown in Figure 21d.

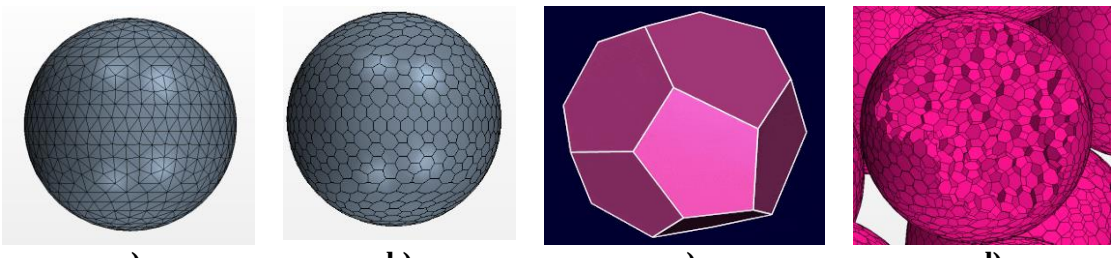

a) **b)** **c)** **d)**

Figure 21: a) Final surface mesh of PCM surface consisting of triangulated elements. b) Final volume mesh of PCM with polyhedral elements c) Polyhedral unit cell used to fill a core volume of a PCM for volume meshing [STAR-CCM+ Documentation, Version 12.04, Siemens, 2017]. d) Volume mesh of a PCM consisting of Polyhedral unit cells.

4 EXPERIMENTAL AND NUMERICAL RESULTS

The following sections present the experimental and numerical results yielded from using the setup described in the previous section. First, the NMR and CFD results for Nitrogen flow through a packed bed will presented. Then the NMR results for Fluorinert flow through a packed bed will be presented together with the CFD results for the three packed beds generated.

4.1 Nitrogen flow through MacroPCM37C

Nitrogen flowed into the PEEK sample holder at an inlet temperature of 45 °C at a flowrate of 270 L/hr. The melt front of PCMs were imaged using a ^{1}H tuned bird cage transmit/receive coil at various times. In the FOV shown in Figure 17a, three sagittal slices and five axial slices were imaged. The sagittal slices were the center sagittal slice of the sample holder and +0.5 cm and -0.5 cm offset from the center slice. The 5 axial slices were at 2 mm, 10 mm, 14 mm, 22 mm and 30 mm from the bottom of the FOV.

4.1.1 Experimental Results

Figure 22 shows the sagittal slices imaged using the methods described in the NMR theory sections. Images were acquired every 7.1 minutes. It was seen that the bed in this field of view completely melted in approximately 57 minutes. The gradual increase in signal strength over time is due to the transition of PCMs from a solid to a liquid phase where it can be deduced that a packed bed height of 50mm melted in approximately 57 minutes. Thermal energy is transferred from the heated nitrogen to the PCMs, melting the PCMs and giving off a stronger signal due to longer T_2 relaxation times. When examined closely, it is seen that the PCMs by the wall melt faster than those by the center of the bed. This indicates a faster flow or preferential flow pathway near the wall, which is consistent with literature [8, 9, 18, 19]. However, due to the unavailability of a ^{7}N tuned coil, the flow of nitrogen could not be imaged and flow pathways can be deduced using the melt front.

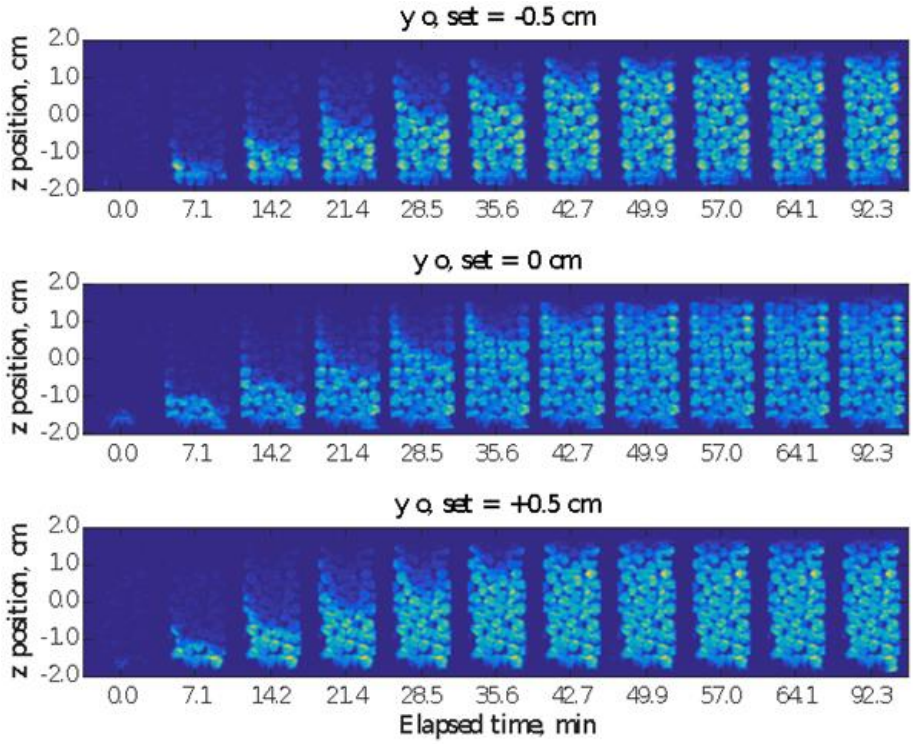

Figure 22: The three sagittal slices imaged every 7.1 minutes shows the gradual increase in signal strength due to PCMs melting over time. Faster melting is seen in some regions indicating preferential flow pathways at these regions.

Figure 23 shows the axial slices imaged that were acquired at various times during the melt. As expected and seen in the sagittal slices, the first axial slices at the bottom of the bed melt faster than slices higher up in the bed. The 2 cm slice shows an increase in signal strength at zero time indicating that the PCMs melted faster than the MRI could image the initial low signal solidified PCMs. Although, the stronger signals on the upper region of the slice at zero time does indicate that there could be preferential nitrogen flow at this region. Furthermore, as seen in the sagittal slices, the axial slices too show relatively stronger signals in PCMs near the wall than those at the center some cases, which indicate faster melting of these PCMs near the wall.

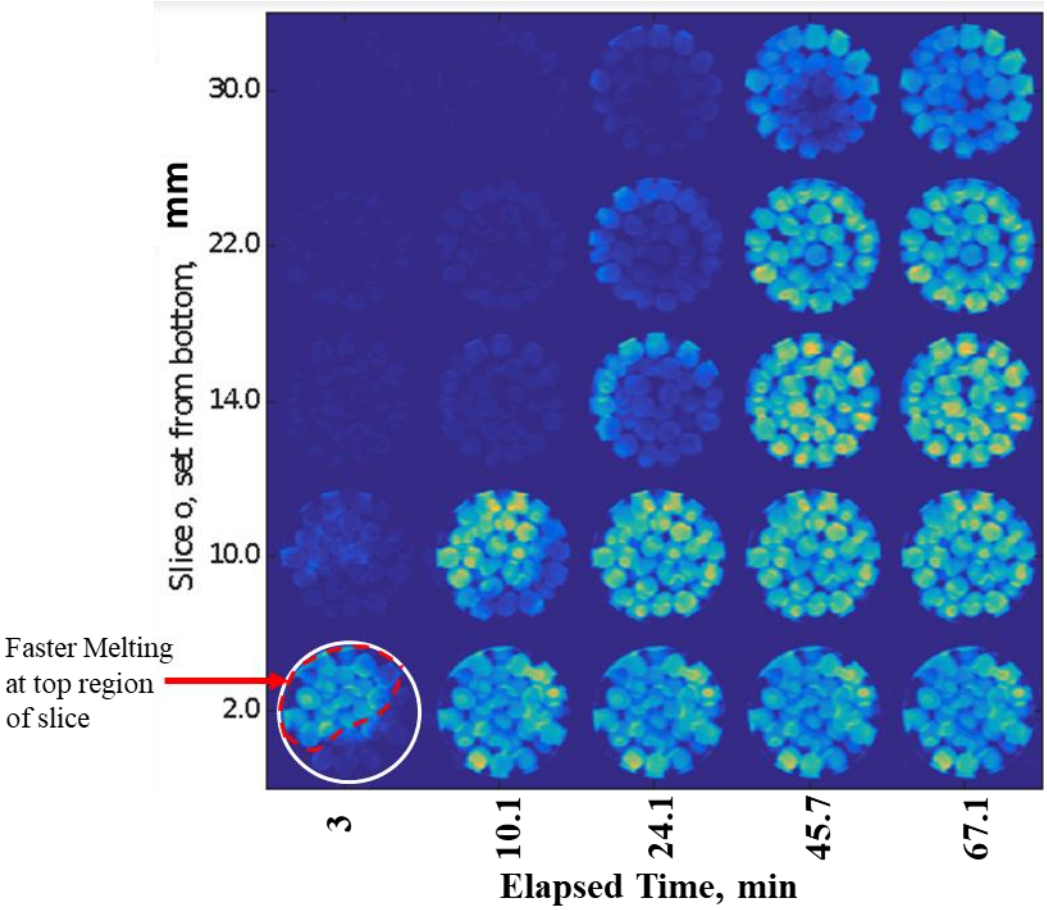

Figure 23: The five axial slices imaged at various times show faster melt regions such as circled region indicating preferential flow pathways at these regions.

4.1.2 CFD Results

Figure 24a shows the FOV of CFD work presented in this section. The axial locations are at the same positions as in the experimental work. The melt profiles, temperature profiles and sagittal slices presented in the CFD work represent the entire 100 mm bed unlike the sagittal slices shown in the experimental work as can be seen in Figure 24b.

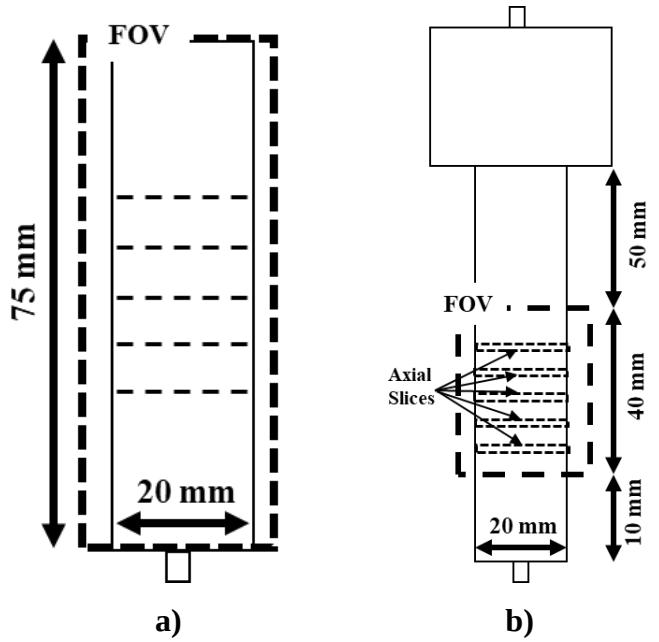

Figure 24: a) FOV used in CFD results. Axial slices at same locations as in experimental data. Melt fraction, Temperature profiles and Sagittal slices represent the entire bed height of 100 mm. b) Experimental FOV showing locations of axial slices presented previously representing only 40 mm of the bed.

Figure 25a shows a melt front height of 100 mm in 55 minutes. This shows a faster melt front height than seen in the experimental work and is determined to be because of the difference in domain sizes. The CFD model used a packed bed diameter and height of 17 mm and 100 mm, respectively while the experimental work used a bed diameter and height of 20 mm and 75 mm. This yielded a CFD modelled bed that had a 37 % less volume than that of the experimental bed and hence a faster melt front can be expected. Yet, other observations can be made in the CFD model such as in Figure 25b, which shows the melt front at an earlier time step (30mins) where it can be seen that there is faster melting in PCMs along the wall as seen in experimental work. The temperature front shown in Figure 25c shows a concave meniscus type temperature front indicating slightly higher temperatures near the wall which suggests that there could be preferential flow pathways along the wall.

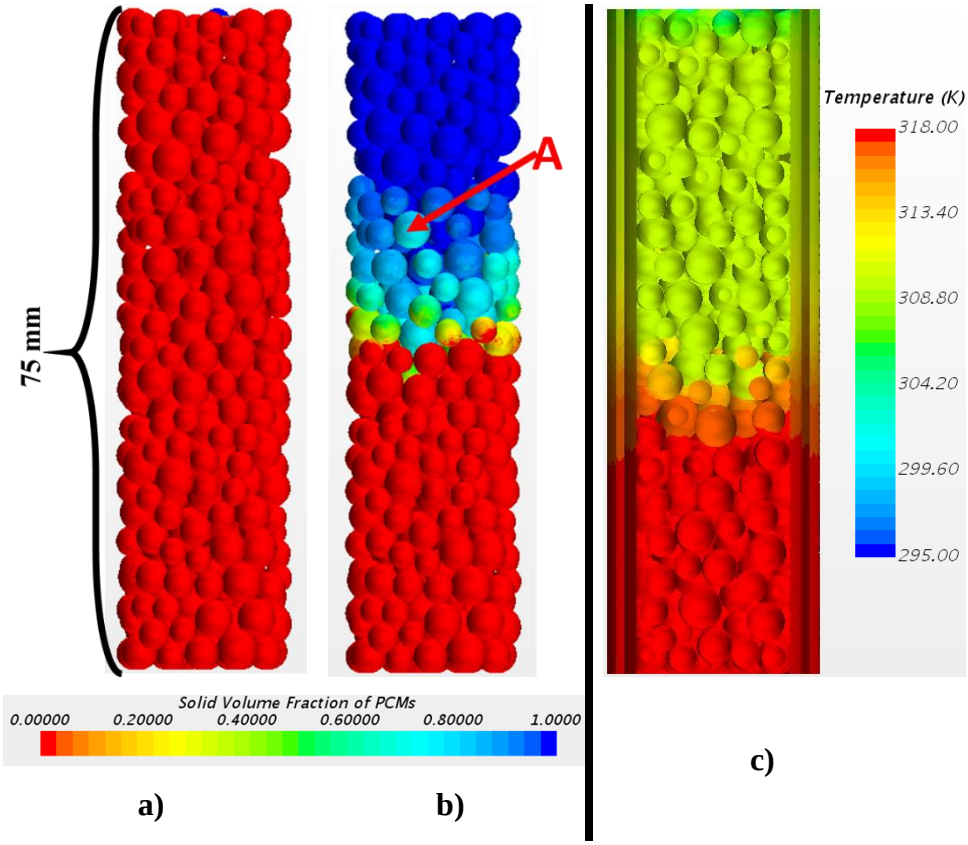

Figure 25: a) Melt fraction at a solution time of 3420s (57 mins) showing a melt height of 75 mm. b) Melt fraction at a solution time of 1560s (26 mins). c) Temperature front at 1560s (26 mins).

Further preferential flow pathways can be determined from examining the melt front in Figure 25b. For example, the PCM marked ‘A’ show slightly faster melting than its neighbors. Therefore, it can be deduced that there is a preferential flow pathway by this PCM, which is confirmed by the streamlines shown in Figure 26, which show a higher number of streamlines by this PCM.

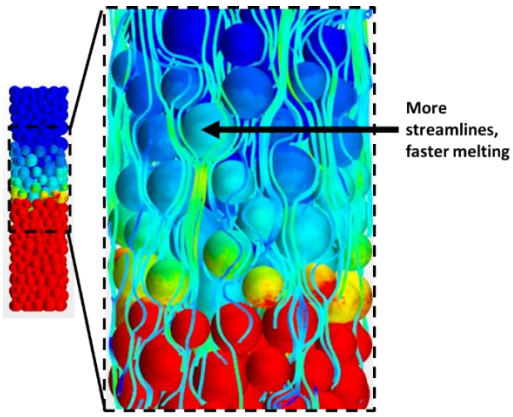

Figure 26: Enlarged detail of melt fraction with streamlines. PCM marked 'A' shows faster melting due to more streamlines.

The sagittal and axial images shown in Figure 27 and Figure 28, captured at the same locations as in experimental work, show preferential flow pathways at various regions including near the walls. In addition, intra-particle temperature melt gradients are seen in the sagittal images such as the PCM marked ‘B’ which shows faster melting on the left side due to faster flow on the left side of the PCM.

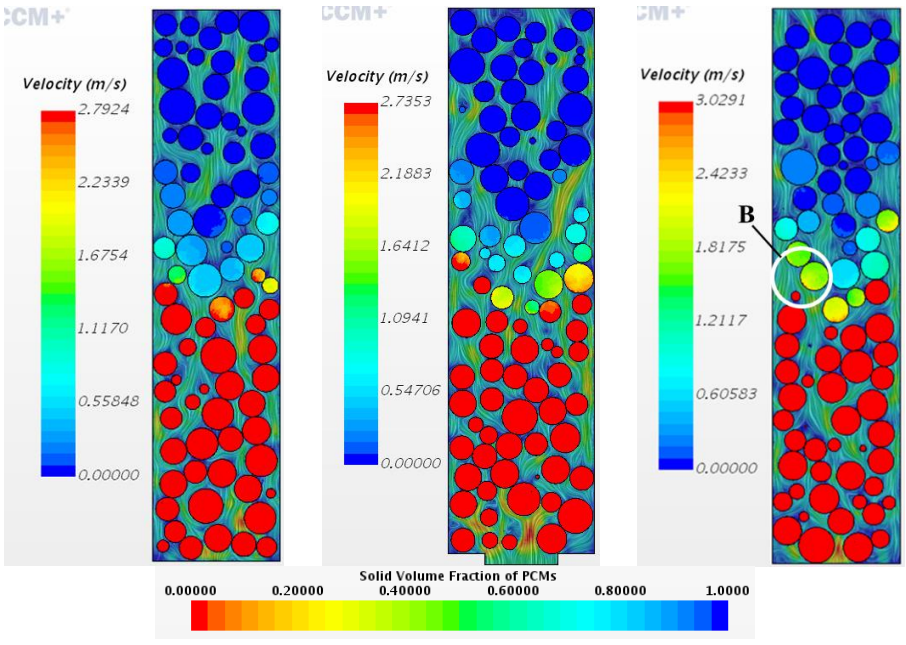

a) **b)** **c)**

Figure 27: Sagittal slices at 30 mins a) -0.5 cm offset sagittal slice b) center sagittal slice. c) +0.5 cm offset sagittal slice.

The axial slices shown unfortunately do not show temperature gradients because all PCMs in the axial slices melted before being saved. However, the axial slices do show preferential flow pathways at various regions including by the wall, which further confirm the results described in in experimental work and literature.

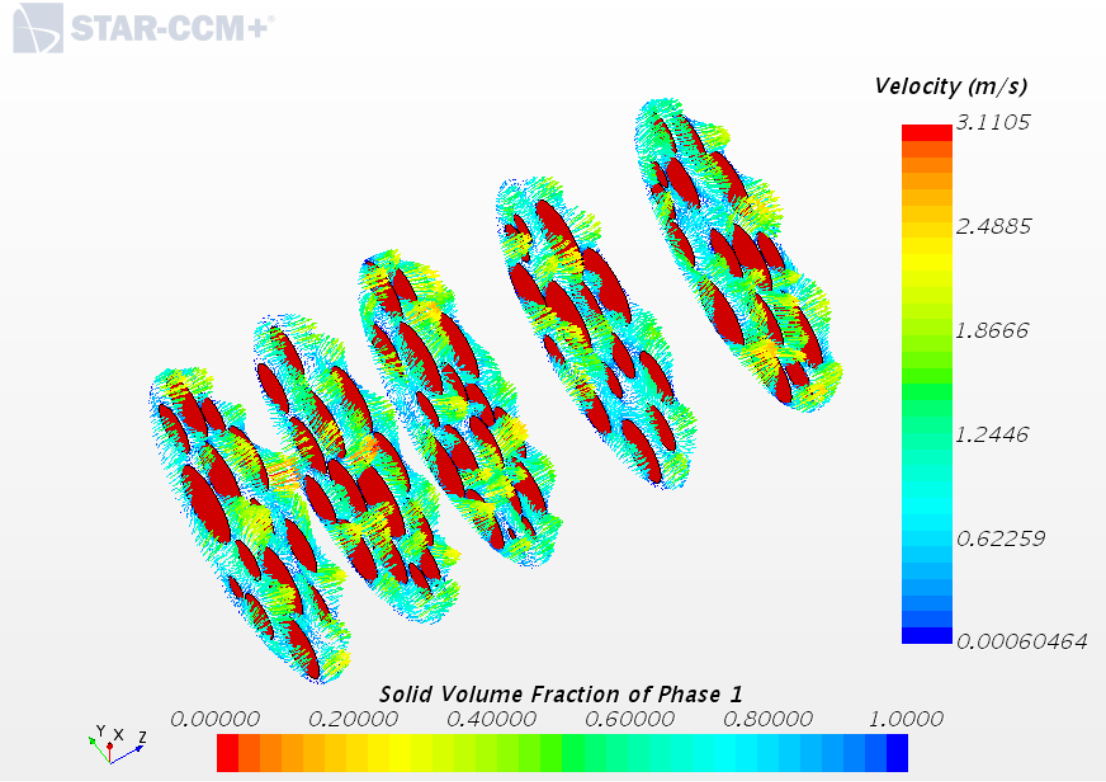

Figure 28: Axial slices at same location as in NMR images at 30 minutes where fully melted PCMs are seen with velocity vectors in the pores around the PCMs.

From the sagittal and axial slices presented, maximum velocities of 3 m/s to 4 m/s were observed. However, this result cannot be verified by experimental work as Nitrogen could not be imaged with available NMR equipment. Yet, the Nitrogen experiments and models offer a stepping stone for further experiments and models discussed in the next section.

4.2 Fluorinert flow through MacroPCM37C

Using the flow loop shown in Figure 15, Fluorinert flowed at 200 mL/hr with an inlet temperature of 38.5 °C through a bed with a diameter of 10 mm filled with MacroPCM 37C. Since Fluorinert was flowed through the packed bed, the available $^{1}H/^{19}F$ dual tuned coil was used to image the melt front as well as the flow velocity. Unlike the previous experiment, this allowed for the clear analysis of flow through the bed including regions of higher flow.

Initially, the coil was tuned to image ^{19}F protons in Fluorinert flow. With the use of a similar PGSE sequence to that described in the NMR theory sections, the velocity of room temperature Fluorinert was imaged. Then, the coil was tuned to image ^{1}H protons and heated Fluorinert flowed through the packed bed to melt the PCMs. As the PCMs melted, the Hydrogen protons in the paraffin gave off stronger signals as discussed in the previous experiment, allowing for a melt front to be imaged using the spin echo sequence described in the NMR theory sections. Three sagittal slices and five axial slices were imaged. The three sagittal slices at the FOV shown in Figure 17b were at the center of the 10 mm cylinder with two more slices being +3mm and -3mm offset from the center slice. The first axial slice was at the center of the same FOV with two more slices above and below the center slice with separations of 5mm between each slice. After the entire bed in the FOV had melted, the coil was re-tuned to image ^{19}F protons and heated Fluorinert flow was imaged for velocity using the same PGSE pulse sequence. For velocity imaging, a center sagittal slice and an axial slice at the center of the FOV was imaged in all three Cartesian directions.

4.2.1 Experimental Results

Figure 29 shows the sagittal velocity in the z-direction at room temperature and at an inlet temperature of 38.5 °C. This bed is vertical in experimental work as seen in Figure 31 but is shown as a horizontal bed due to the way it was processed. Maximum velocities of 8 mm/s are seen at regions by the wall indicating preferential flow pathways along the walls as discussed in literature [8, 9, 18, 19]. Consider the large local pore

shared by the PCM marked ‘A and ‘B’. This relatively larger pore shows a faster flow region consistent with the channeling effect phenomenon.

These velocity images also have sufficient resolution to show local Hagen-Poiseuille type velocity profiles, which can be seen by the local maximum velocities at center of various pores consistent with literature. As can be seen from Figure 29, Velocity imaging was done before the PCMs melted with room temperature Flourinert and after the PCMs melted with heated Flourinert. There were a few reasons this was done. The first reason was to ensure that any unsettled PCMs do settle so that the pores sizes do not change during the actual melting of PCMs. This ensures the condition that a fixed bed is imaged. This settling of PCMs is shown by the appearance of the PCM marked ‘C’ in only the heated flow image of the Figure 29. This change in the pore structure causes changes in flow velocities between the unheated and heated images and is attributed to the change in maximum velocities discussed later. Another reason velocity imaging is done pre- and post-melt is to allow for the liquid phase to develop fixed preferential flow pathways that do not change. This ensures that the change in direction of flow pathways observed is solely due to fixed solid phases and not due to an apparent restructuring of the solid phase.

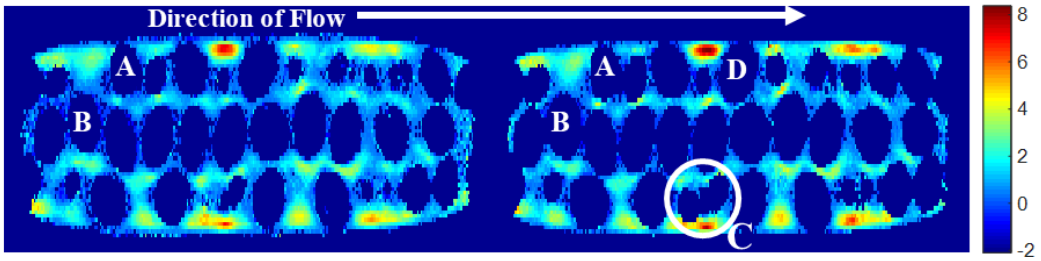

Figure 29: Sagittal z-direction velocity maps of Fluorinert flow. Flow direction from left to right. a) Velocity with original scaling. b) Velocity maps scaled between -4 mm/s and 4 mm/s.

Another observation accurately captured by the velocity images is the change in direction of flow pathways. This is clearly seen in the pores before the PCM marked ‘D’ in Figure 29 and Figure 30. The z-direction flow in the pore before this PCM indicates a

high velocity but this flow pathway is blocked by the PCM marked ‘D’. The Fluorinert must flow around this PCM in the x- and y-direction. When Figure 30 is examined, a flow component is observed in the x- and y-directions at this pore space behind the PCM marked ‘D’.

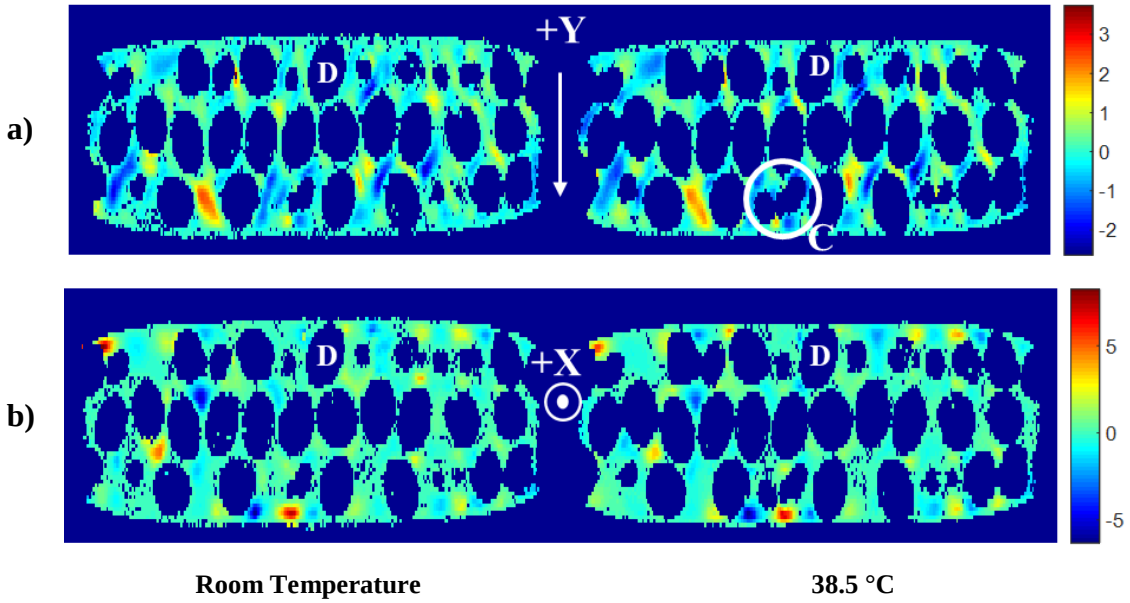

Figure 30: a) Sagittal y-direction velocity maps b) Sagittal x-direction velocity maps

Figure 31 shows the sagittal slices of the melt front at various times. The center sagittal slice shown in Figure 31b correspond to the same location of the velocity image shown in Figure 29 and Figure 30, where the same PCMs marked ‘A’ and ‘B’ show faster melting due to the high flow region seen in Figure 28 and Figure 30. The melt front images also show intra-particle melt gradients with faster melting on sides of faster flow regions. Consider the PCM marked ‘D’, which shows faster melting at the lower region of the PCM. When this is coupled with the velocity image shown below, a faster flow region is seen at the pore before this PCM. Another result obtained from the sagittal images is the time it takes to melt the bed. Since the FOV of the sagittal slice is 40 mm at a location 20 mm from the inlet, it can be deduced that 60 mm of the bed melted in 41 minutes.

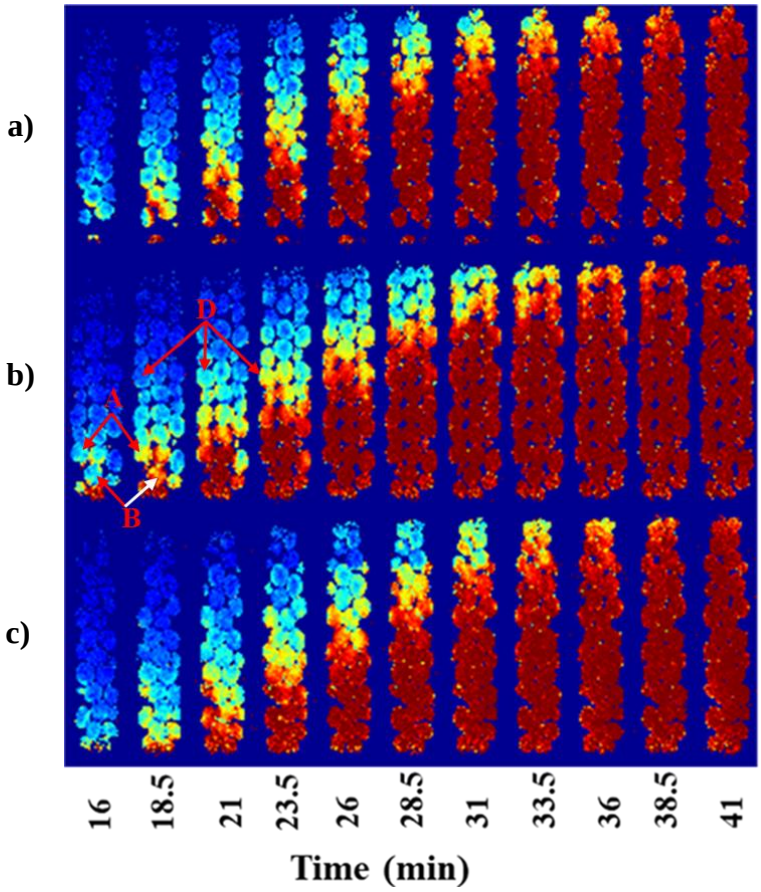

Figure 31: Sagittal Melt front of PCMs every 2.5 mins. a) -0.3cm offset Sagittal b) Center Sagittal c) +0.3cm offset Sagittal

Figure 32 shows the axial velocity in all directions, which clearly show the preferential flow pathways along the wall seen in sagittal slices indicated by faster flow regions along the wall. Seen further is the settling of PCMs between the unheated and heated flows labeled as 'C'. The axial images provide an interesting result that is not seen in the sagittal images where indications of conservation of mass is seen. This is indicated by the relatively lower z-direction velocities at the faster flow regions in x- and y-directions while at relatively faster z-direction velocity regions, there are relatively low x- and y-directions flows.

The conservation of mass is examined quantitatively by using the axial velocity data to calculate the flowrate in the z-direction axial slice, which was then compared with

the known flowrate of 200 mL/hr that the Fluorinert was pumped. This volumetric flowrate was calculated by multiplying the pixel area with the respective z-direction velocity in that pixel, which yielded volumetric flow rates for each pixel. The volumetric flow rate in each pixel was then summed to yield a volumetric flowrate of 188.5 mL/hr which is 93% of the actual flowrate of 200mL/hr. This variation in flowrate from the actual flowrate is suspected to be due to limitations in NMR data processing. More specifically, consider a pixel right by a PCM boundary or wall. Although this pixel averages out to give a zero velocity, this pixel could have actually had non-zero velocities within the pixel. In addition, when the data is processed a calculation threshold is specified to remove the noise obtained in the images, which in turn can zero out pixels that show velocities.

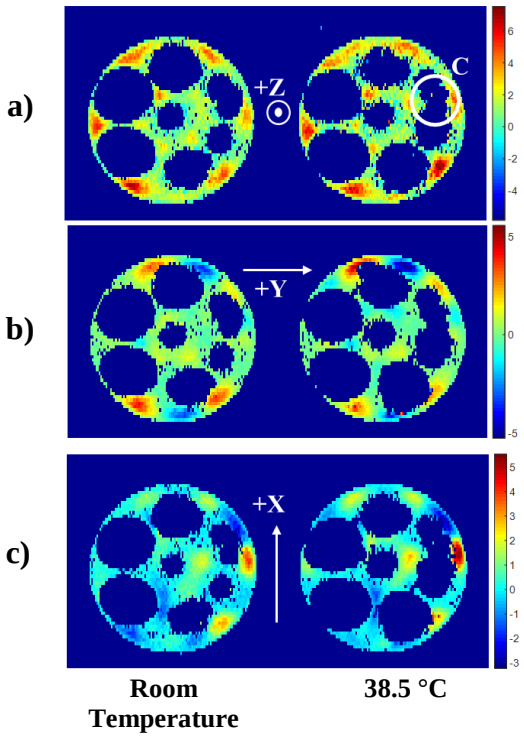

Figure 32: a) Axial slices with z-direction velocity. b) Axial slice with y-direction velocity. c) Axial slices with x-direction velocity

Figure 33 shows the axial melt fronts at the five locations of the FOV shown in Figure 17. As expected, the lower slices melt before the higher slices. The axial velocity

images shown in Figure 32 correspond to the location of slice 3 in Figure 33. Intra-particle melt gradients are seen in these axial images with faster melting on sides of faster flow. Consider the circled PCM in Figure 33, which shows faster melting on the top right corner of the PCM. If the pore region by this PCM is inspected in Figure 32, a faster flow region is seen at the pore near the top right corner of this circled PCM.

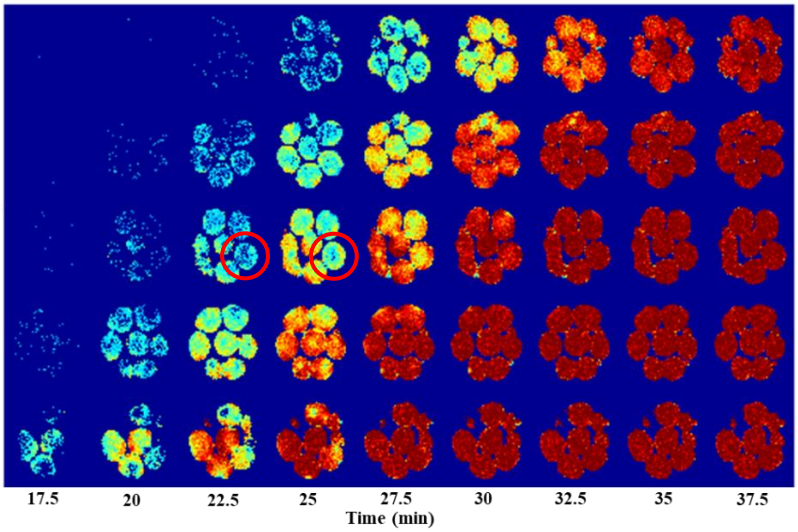

Figure 33: Axial melt front at 5 different slices every 2.5 minutes. Faster melting is seen in regions of preferential flow pathways

Table 4 shows the maximum velocities seen in the sagittal slices of Figure 29 and Figure 30 and the maximum velocities seen in axial slices of Figure 32. The change in maximum velocities is suspected to be caused by the settling of PCMs during the initial Fluorinert flow.

Table 4: Maximum velocities obtained from sagittal and axial images. The change in temperature is caused by the settling of PCMs.

	Maximum Velocity (mm/s)			
	Sagittal		**Axial**	
Direction	**Unheated**	**Heated**	**Unheated**	**Heated**
z	7.1	8.7	6.9	7.5
y	3.7	2.3	4.1	5.6
x	8.2	6.7	4	5.5

4.2.2 CFD Results for Bed of Monodisperse Spheres with a Diameter of 3.77 mm

Using Star CCM+'s melting/solidification models discussed previously, the PCM solid fraction volume was observed over time to determine how much of the bed melted. For this bed, three sagittal slices were made at the center of the bed and with +0.3 cm and -0.3 cm offset slices from the center. In addition, 5 axial slices are presented with the first axial slice at the center of the bed with two more slices above and below the center slice with separations of 5 mm between each slice. Figure 34a more clearly shows the FOV of CFD work presented in this section. The axial locations are at the same positions as in the experimental work. It must be noted that the melt profiles, temperature profiles and sagittal slices presented in the CFD work represent the entire 85 mm bed unlike the 40 mm sagittal slices shown in the experimental work.

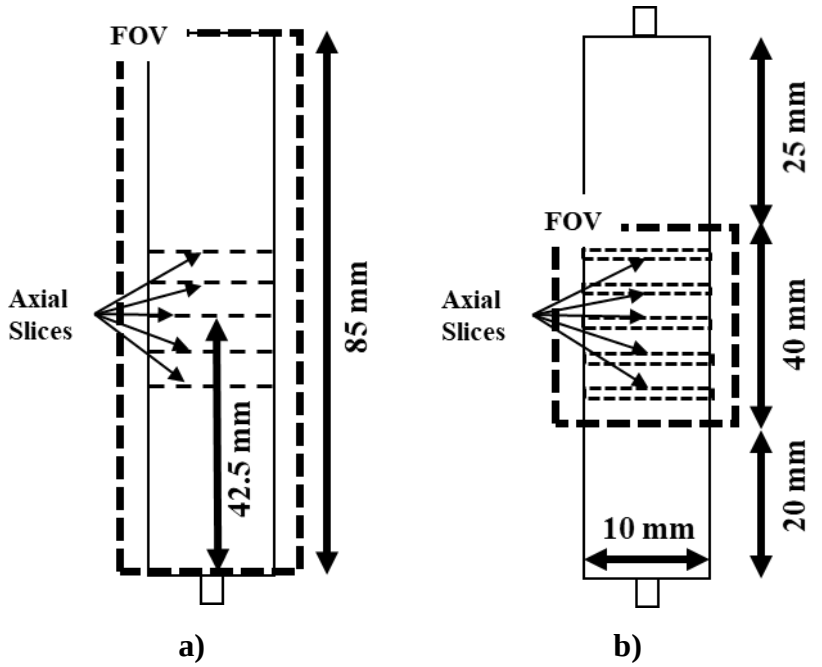

Figure 34: a) FOV used in CFD results. Axial slices at same locations as in experimental data. Melt fraction, Temperature profiles and Sagittal slices represent the entire bed height of 85 mm. b) Experimental FOV showing locations of sagittal slices and axial slices presented previously representing only 40 mm of the bed.

Figure 35a show the melt front through the packed bed at a physical time of 2460s (41 mins). The fully melted PCMs are represented in red while the solid PCMs are represented in blue and any colors between these colors represent PCMs during melt. The model showed that approximately 54 mm of the bed completely melted in 41 minutes. This is qualitatively similar to the experimental result discussed previously. However, when this bed was further examined, an anomaly was seen where faster melting is seen at the center of the bed. This indicates that there is faster flow in the central region of the bed, which is inconsistent with experimental data. Figure 35b and Figure 35c show the temperature of the PCMs at a time step of 60s and at 41 minutes, respectively. The temperature front at 60s shows more contrast, indicating a faster change in temperature at the center of the bed.

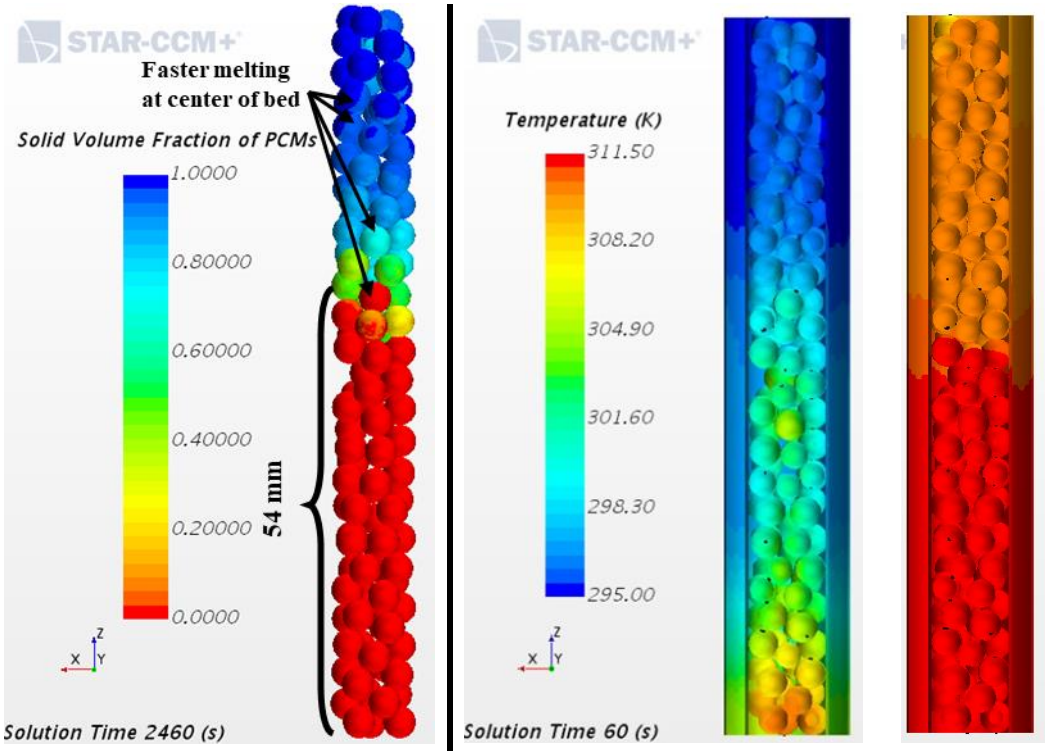

Figure 35: a) Melt front at a solution time of 2460s (41 min). b) Temperature front at a solution time of 60s. c) Temperature front at a solution time of 2460s (41 min).

Sagittal and axial slices help explain this anomaly. Figure 36 shows the center sagittal slice, which clearly shows poor packing of PCMs, causing larges pore to form at

the center of the bed. As a result, Fluorinert flow is concentrated at these pores and hence at the center of the bed, which causes faster melting at the center of the bed. Therefore, the preferential flow pathways along the walls seen in experimental results are not seen here.

However, an observation that is consistent with experimental data is the melt gradient seen in the PCMs. For example, consider the PCMs on either side of the large pore seen in Figure 36a. These PCMs show a melt gradient with the side closest to the large pore melting faster. This is consistent with experimental data as the higher flow sides melt that respective side of the PCMs faster.

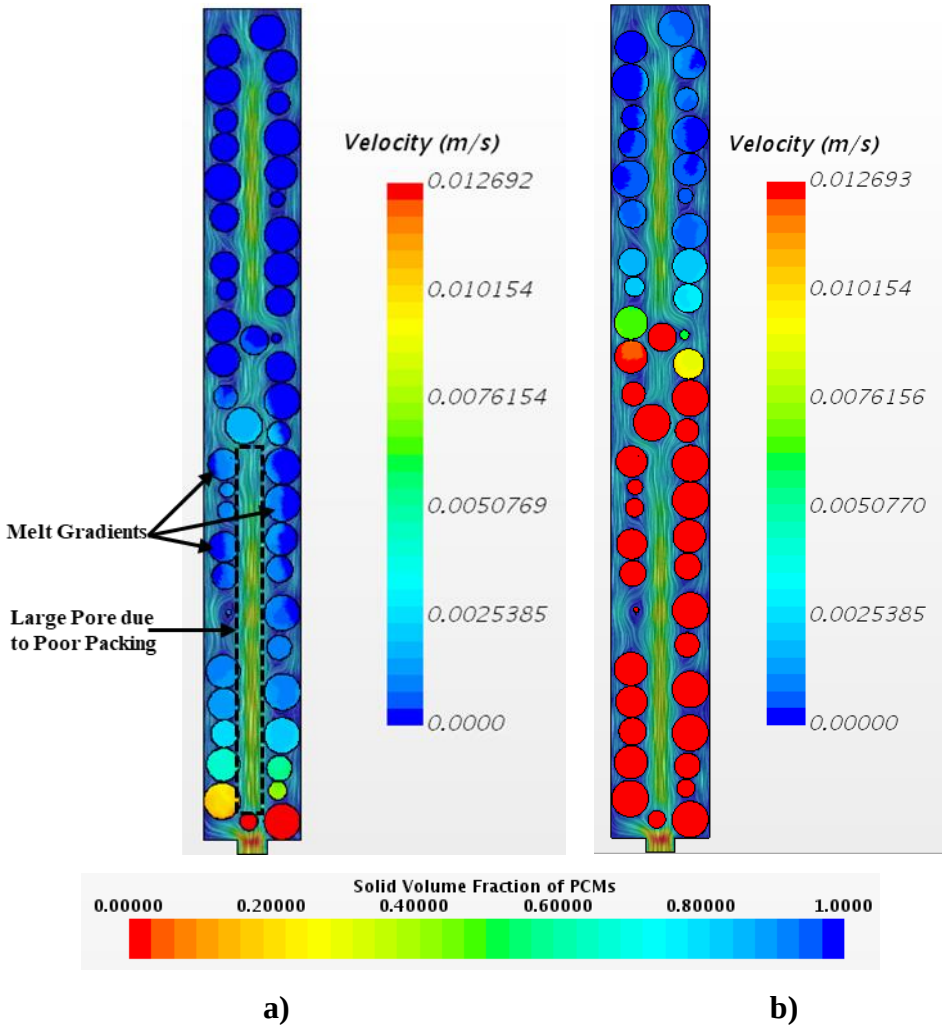

Figure 36: a) The center sagittal slice at a solution time of 540s where intra-particle melt gradients can be seen. b) Same sagittal slice at a solution time of 2460s (41 min)

This effect is further confirmed by Figure 37a, which shows the axial slices of the melt front together with velocity vectors of Fluorinert flow. The PCM marked ‘E’, for instance, shows a melt gradient with faster melting on the side of faster flow. These figures also show the concentration of flow at the center due to poor packing and hence the faster melting of PCMs near the center of the bed.

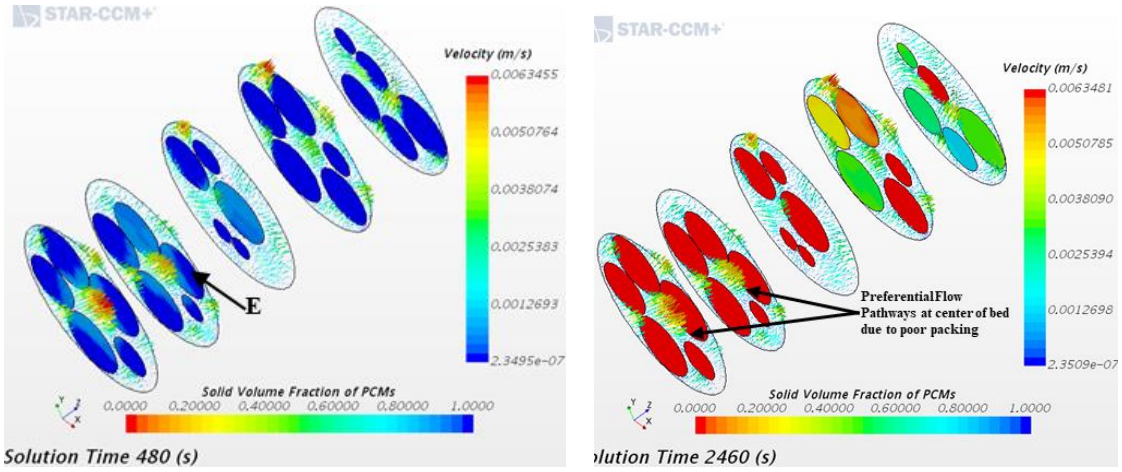

a) **b)**

Figure 37:(a) The axial slice at a solution time of 480s to clearly show intra-particle melt gradients such as in the PCM marked 'F'. (b) The melt fraction in the same axial locations at a solution time of 2460s (41 mins).

The sagittal slice in Figure 36 report maximum velocities of 8 mm/s while the axial slices in Figure 37 report maximum velocities of 6 mm/s, which are similar to the maximum velocities found in the experimental data. The reader is directed to ignore the maximum velocity shown in the sagittal slice as this takes into account the velocity at the inlet, which is not considered in the experiment.

The packing of this bed was done repeatedly to try to eliminate the poor packing but this was unsuccessful as a large pore formed nonetheless. This is the primary reason that other approaches were explored and two other packed beds were modelled.

4.2.3 CFD Results for Bed of Spherical Particles with a Gaussian Distribution in Diameters

The packed bed with constant spherical diameters caused poor packing and hence, yielded data that were not consistent with literature and experimental data. Therefore, the bed discussed in this section was modelled where the particles had a Gaussian distribution in spherical diameters. The same information was gathered as in the previous section. For this bed, three sagittal slices were made at the same locations as before; however, the five axial slices presented are at a lower location of the bed in order to capture the melt front. The five axial slices are at 3mm, 10mm, 15mm, 20mm, and 25mm from the inlet of the bed. Figure 38a more clearly shows the FOV of CFD work presented in this section. The axial locations are closer to the inlet unlike in the experimental work. Similar to the previous model, the melt profiles, temperature profiles and sagittal slices presented in the CFD work represent the entire 85 mm bed unlike the 45 mm sagittal slices shown in the experimental work.

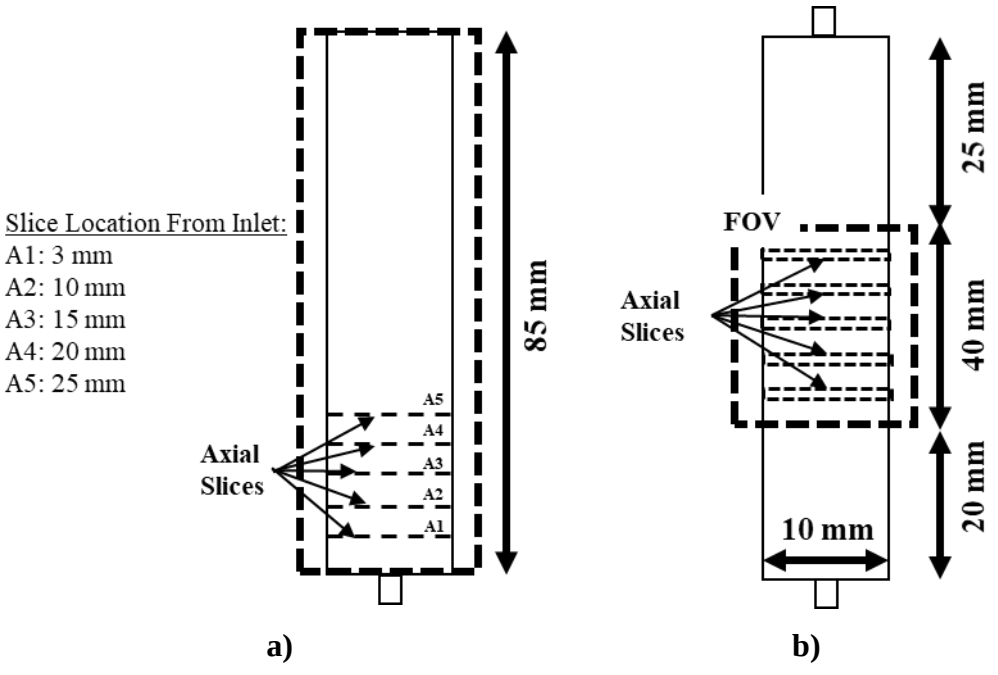

Figure 38: a) FOV used in CFD results. Axial slices closer to the inlet unlike in experimental data. Melt fraction, Temperature profiles and Sagittal slices represent the entire bed height of 85 mm. b) Experimental FOV showing locations of sagittal slices and axial slices presented previously representing only 40 mm of the bed.

Figure 39a shows a melt front height of 18 mm in at a solution time of 2460s (41 mins). This bed shows no anomalies in packing when compared with the previous bed, which indicates that there is better packing of PCMs in this bed. Furthermore, if observed carefully, faster melting is seen along the walls of the bed. This is indicative of faster flow regions or preferential flow pathways along the wall, which is consistent with experimental data and literature. This effect is further seen in Figure 39b, which shows the temperature front at 60s where the PCMs along the left wall have a higher temperature than those at the center. Shown here is also the temperature front at a solution time of 41 minutes.

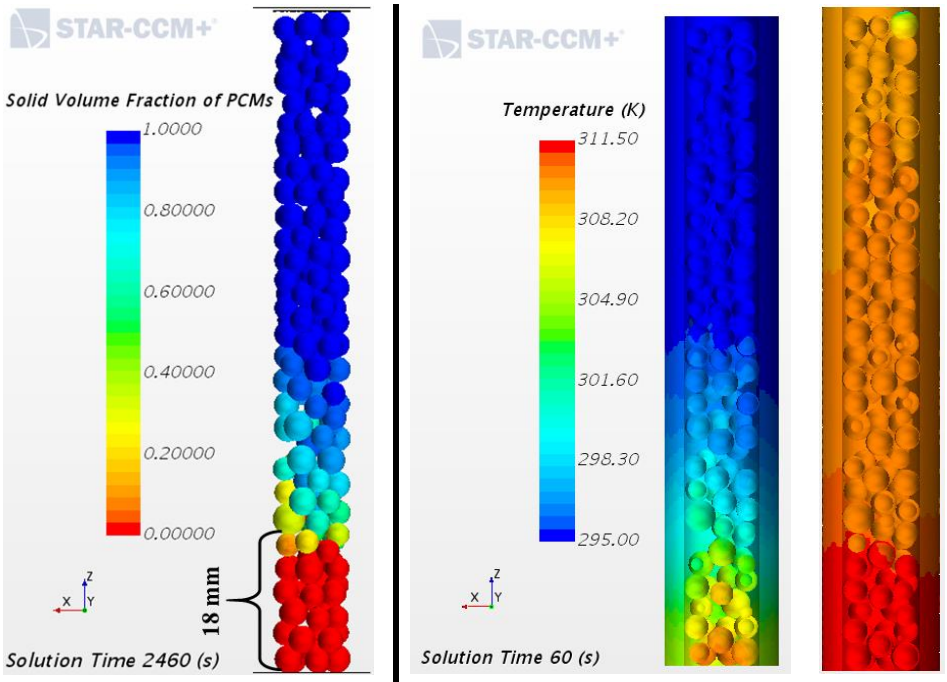

Figure 39: a) Melt front at a solution time of 2460s (41 mins) b) Temperature front at a solution time of 60s. c) Temperature front at a solution time of 2460s (41 mins)

Another successful result from these models were the melt and temperature gradients visible in some PCM surfaces such as in Figure 40, which shows the velocity streamlines around the PCMs. Consider the PCM marked ‘F, which shows a melt gradient with faster melting on the right side. As can be seen there is a higher

concentration of streamlines on the right side, which indicates more mass flux and hence faster melting.

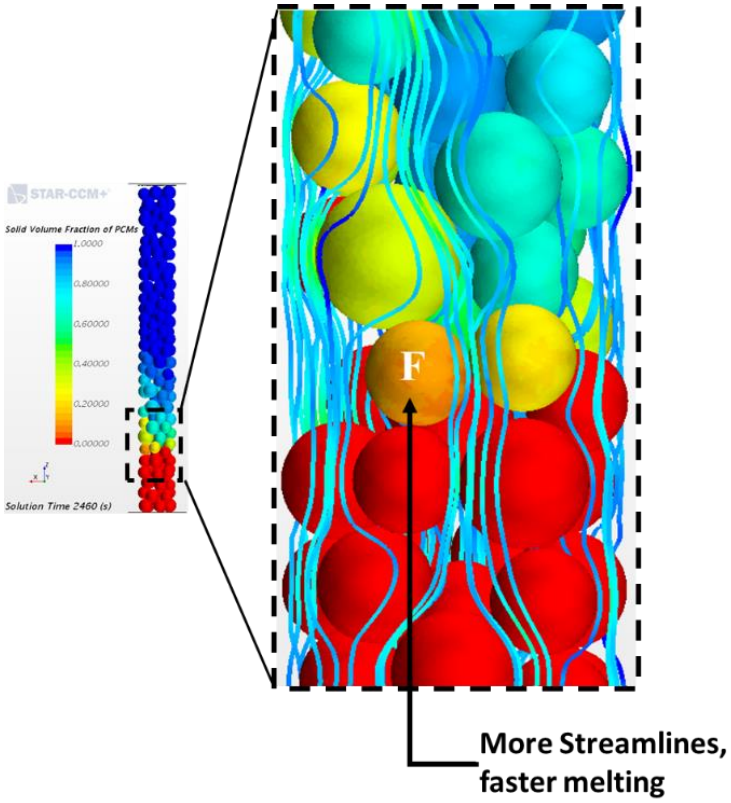

Figure 40: Enlarged detail of the melt fraction with streamlines. Areas of more streamlines show faster melting such by PCM marked 'F'.

As seen in the previous model, this melt gradient is also seen in the sagittal slices presented in Figure 41a. It is believed that better intra-particle melt gradients can be seen more distinctly if the CFD model saved the slice images more frequently than every 60 seconds as done in this work. However, slight gradients can be seen in the PCM marked ‘H’ in Figure 41a, for instance, where higher melting is seen on the bottom left and right of the PCM due to higher flow regions on these respective sides. Figure 41 also shows preferential flow pathways along the walls indicated by the faster velocities along the wall in all three slices. This effect is now seen as there are no internal large pores and therefore, better packing than in the previous model.

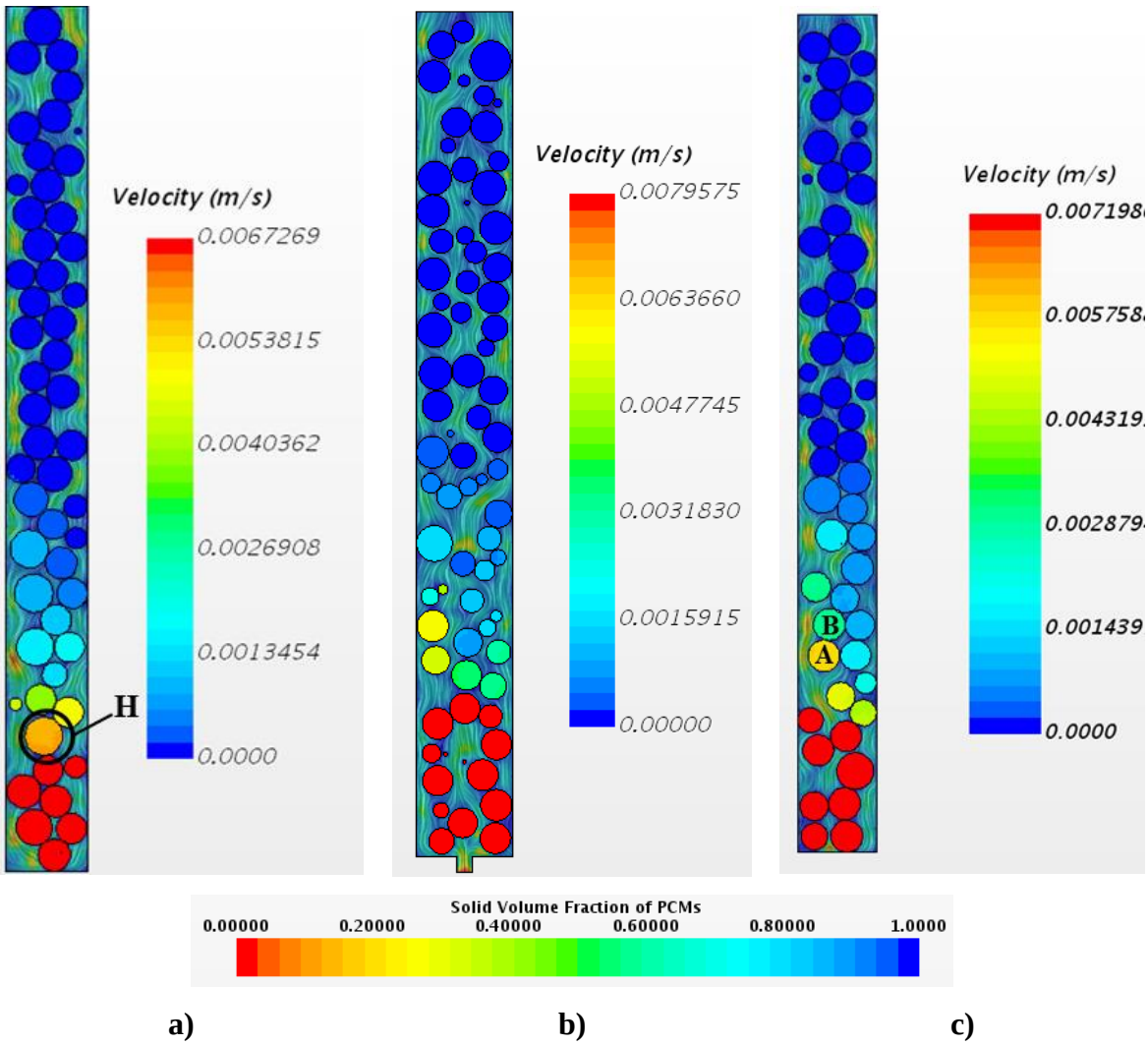

Figure 41: a) -0.3cm offset sagittal slice at a solution time of 2000s where intra particle melt gradients are seen in PCM marked 'H'. b) Center sagittal slice at a solution time of 2460s (41 mins) b) +0.3 cm offset sagittal slice at a solution time of 2160s where PCMs marked ‘A and ‘B’ melt faster due to larger nearby pore

Recall the PCMs marked ‘A’ and ‘B’ in the experimental data, which showed faster melts than its neighbors due to the presence of local larger pores and hence, higher flow near these PCMs. The PCMs marked ‘A’ and ‘B’ in Figure 41c also show a similar process. These PCMs melt faster than their neighbors beside it due to the presence of a relatively large pore and hence higher flow by these PCMs. The similarity in flow and pore structure is further seen in Figure 42 where Figure 42a show a quiver plot of the experimental velocity data, which is a 3D representation of the velocity vectors

calculated from the velocity data in all directions. Figure 42b shows the velocity vectors calculated from the model and similar qualitative flow dynamics can be seen.

a)

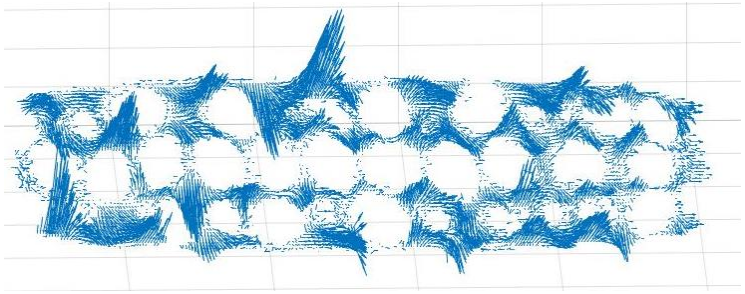

b)

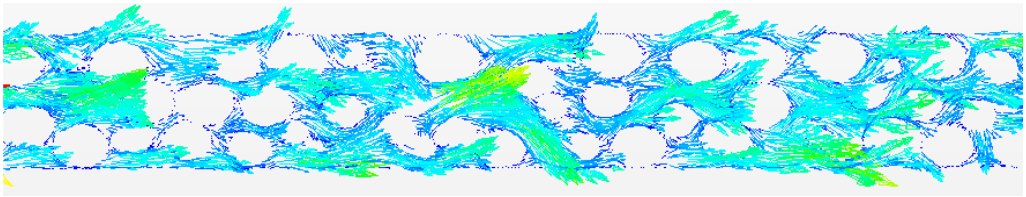

Figure 42: (a) A 3D plot of velocity vectors developed from the experimental data at center sagittal. (d) 3D velocity vector plot at the center sagittal obtained from the CFD model

The preferential flow pathways along the wall is further confirmed by the axial slices shown in Figure 43. However, it can be noticed that the first axial slice actually shows a faster flow region at the center. This is because the first axial slice is only 3mm from the inlet and therefore, inlet effects are captured here unlike the NMR images. However, in the higher axial slices, faster flow regions along the wall are more prevalent. These slices also show faster melting of PCMs near faster flow regions such as the PCM marked ‘I’.

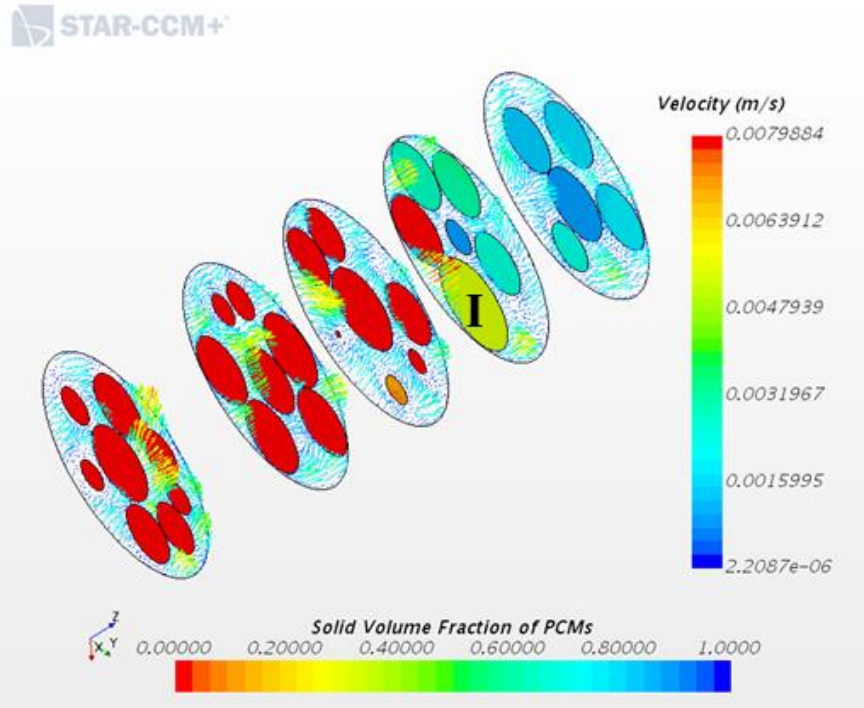

Figure 43: Axial slices at locations of 3mm, 10mm, 15mm, 20mm and 25mm at a time step of 2460s (41mins) that show the melt front and velocity vectors of flow

In the sagittal and axial slices, maximum velocities in the range of 6 mm/s to 7 mm/s are seen, which are similar to the velocities obtained from the experimental data. Again, the reader is directed to ignore the maximum velocities shown in the center sagittal slice and the axial images because the sagittal slice and the first axial slice include the inlet effects that are not captured in the experimental data. In summary, this packed bed model is a good complement to the NMR data only although only 18 mm of the bed melted, which will be discussed further later.

4.2.4 CFD Results for Bed of Non-Spherical Particles with a Gaussian Distribution in Diameters

Literature has shown that particle geometry has effects on the flow dynamics within a packed bed [22, 24]. Therefore, the bed discussed in this section was generated using three non-spherical volumes, discussed previously, that all have a Gaussian Distribution in diameters. Similar information was gathered in this model with the same

three sagittal slice locations as before; however, four axial slices were gathered at new locations to capture the melt front. The four axial slices are at 2 mm, 6 mm, 10 mm and 15mm from the inlet of the bed. Figure 44a more clearly shows the FOV of CFD work presented in this section. The axial locations are closer to the inlet unlike in the experimental work. Similar to the previous models, the melt profiles, temperature profiles and sagittal slices presented in the CFD work represent the entire 85 mm bed unlike the 40 mm sagittal slices shown in the experimental work.

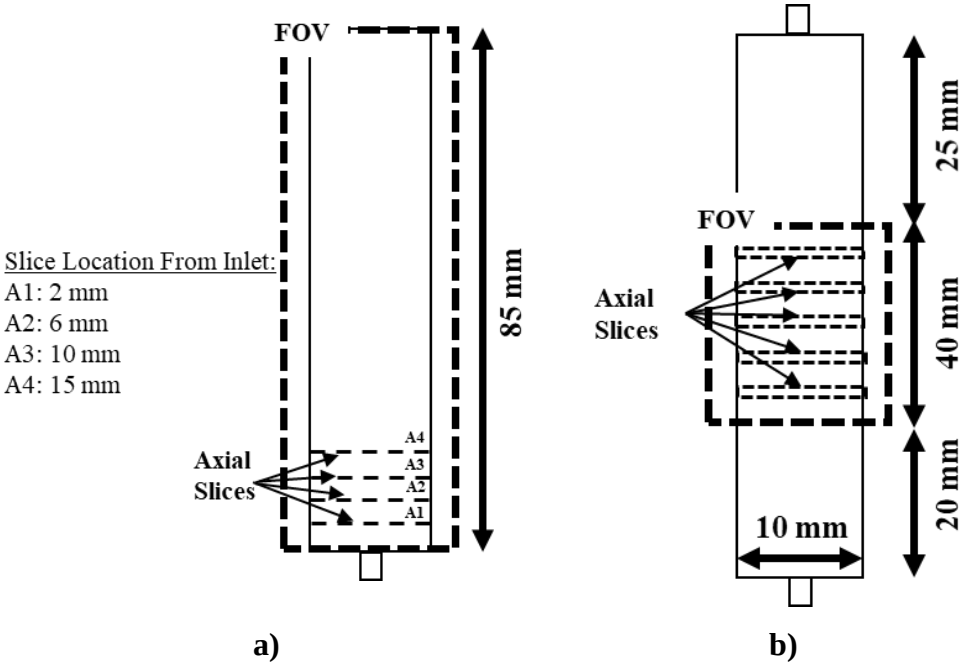

Figure 44: a) FOV used in CFD results. Axial slices closer to the inlet unlike in experimental data. Melt fraction, Temperature profiles and Sagittal slices represent the entire bed height of 85 mm. b) Experimental FOV showing locations of sagittal slices and axial slices presented previously representing only 40 mm of the bed.

The melt front of this bed is shown in Figure 45a, where approximately 13.5 mm of the bed melted in 41 minutes. This was the reason the axial slices were moved to a lower location than that of the experiment so that the melt fraction could be captured. Furthermore, this bed too, does not show any packing anomalies and shows a melt front that is faster along the walls of the bed indicating that there is preferential flow pathways along the wall as seen in experimental results and literature [22, 24]. This is also seen in

the temperature front image shown in Figure 45b where the PCMs along the wall show higher temperatures than those at the center. Shown in Figure 45c is also the temperature front a time of 41 minutes.

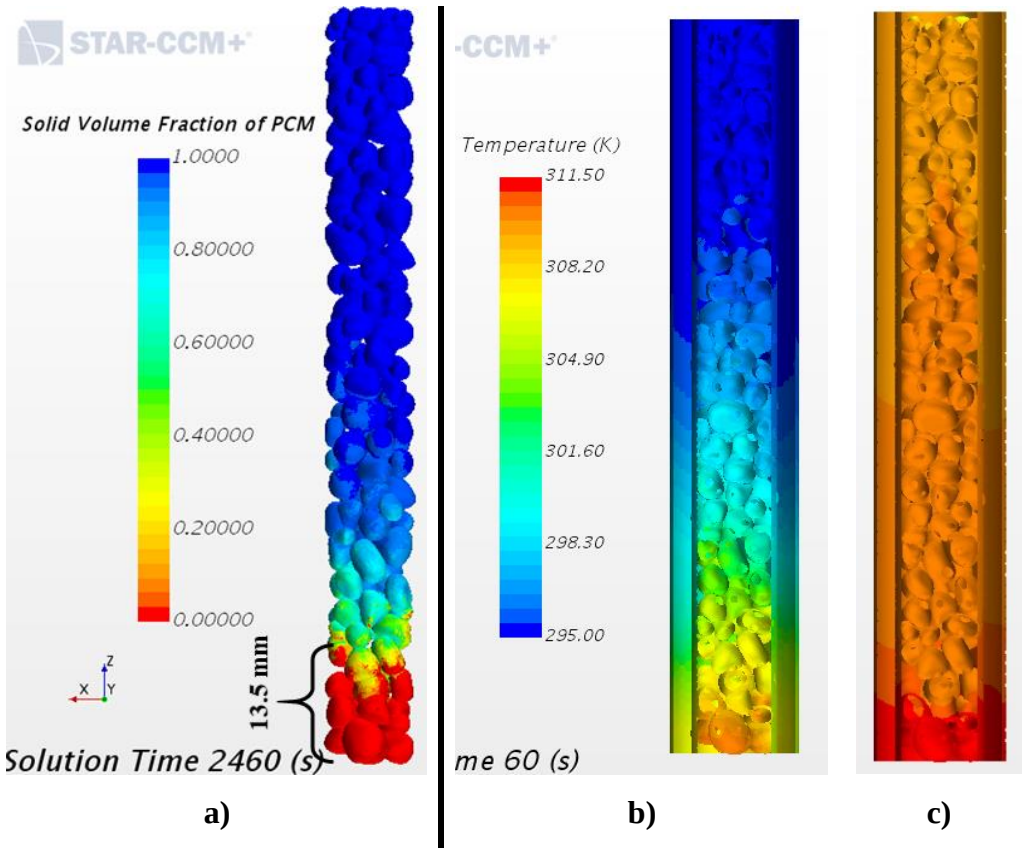

Figure 45: a) Melt front at a solution time of 2460s (41 mins). b) Temperature front at a solution time of 60s. c) Temperature front at a solution time of 2460 (41 mins).

Similar to the Spherical Gaussian bed, melt and temperature gradients are seen in the PCM surfaces. In fact, better melt gradients are seen such as in the PCM marked ‘J’ which shows faster melting on the bottom of the PCM which is then examined further by using velocity streamlines as shown in Figure 46. This figure shows a higher concentration of flow by the bottom of the PCM, represented by the higher number of streamlines which causes faster melting at the bottom of the PCM.

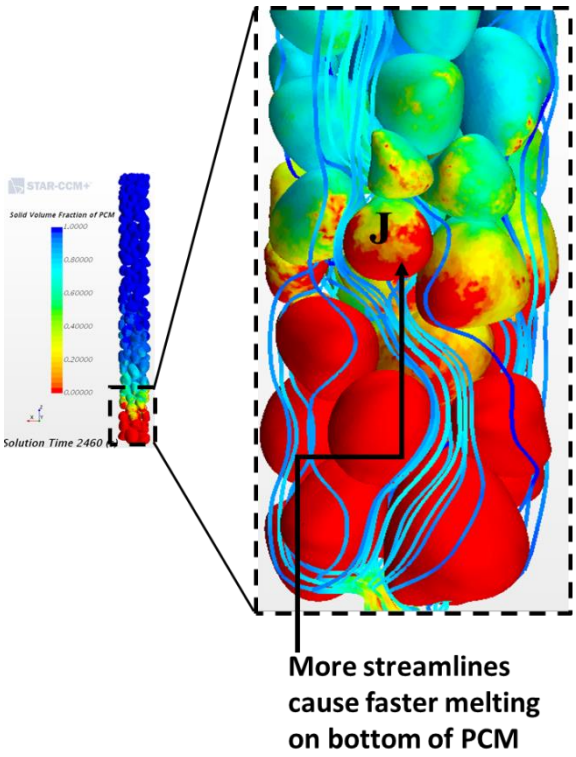

Figure 46: Enlarged detail of the melt fraction with streamlines. PCM marked 'J' shows melt gradient with faster melting at the bottom due to faster flow indicated by more streamlines at the bottom of the PCM

These effects are further confirmed by the sagittal slices shown in Figure 47. For instance, the PCM marked ‘K’ shows a melt gradient with faster melting on the bottom of the PCM. This makes sense as there is higher flow on the bottom of this PCM. Also, preferential flow pathways along the wall are seen in the sagittal slices, especially in Figure 47a and Figure 47c. It must be noted that there are preferential flow pathways along the wall in the center sagittal slice although it is not clearly seen because the higher velocity at the inlet conceals the display of the high velocities near the wall. Recall the PCMs labeled ‘A’ and ‘B’ in the NMR experiments and Spherical Gaussian model. Similarly, there are PCMs by relatively large pores that show faster melting than their neighbors due to local higher lows. These PCMs are labeled ‘A’ and ‘B’ in Figure 47c.

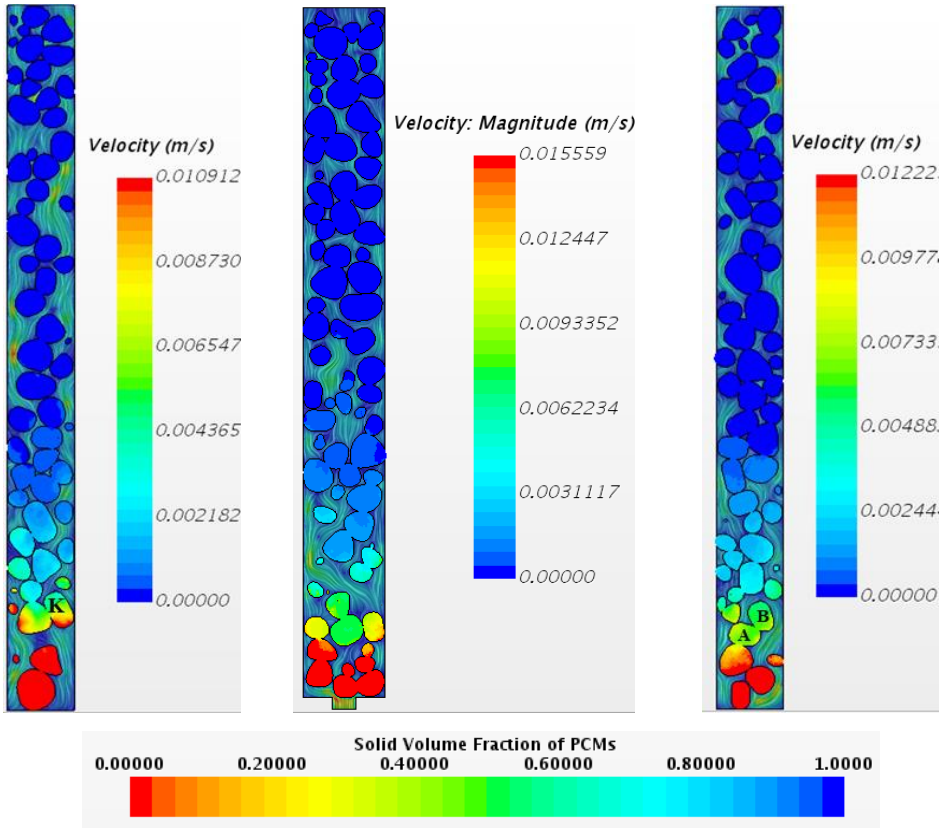

a) **b)** **c)**

Figure 47: The three center sagittal slices at solution time of 2000s (33mins) where the melt fraction and the velocity in the pores is seen. Note that all melt fraction shown is scaled to the same color bar. a) -0.3cm offset sagittal b) center sagittal c) +0.3cm offset sagittal

The axial slices shown in Figure 48a further confirm the preferential flow pathways along the wall of the bed. Recall that the lowest axial slice in the Spherical Gaussian bed showed a preferential flow pathway at the center of the bed due to the inlet effect. This poses the question as to why the same effect is not seen in the lowest axial slice of this bed, which is only 2mm from inlet. This question is resolved if the center sagittal slice is examined at the inlet where a PCM lies directly above the inlet blocking any flow through the center. The axial slices also show melt gradients, such as in the PCM marked ‘L where faster melting is seen on the left side due to faster flow regions on this side of the PCM. These gradients further confirm the intra-particle melt gradients seen in the NMR images presented previously.

a)

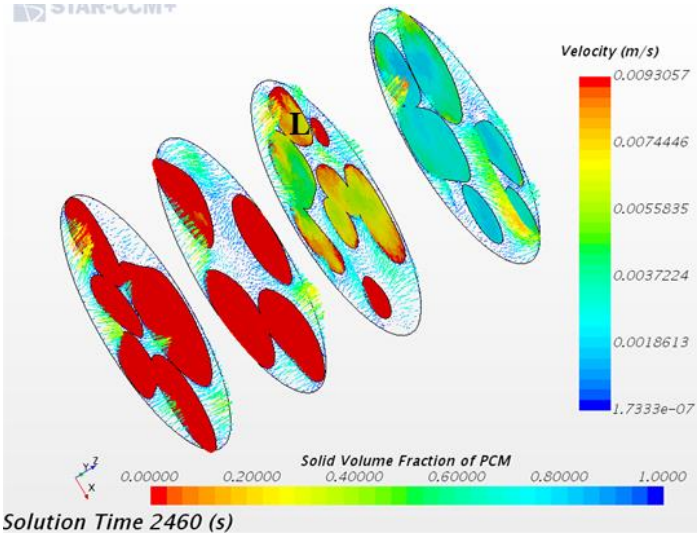

b)

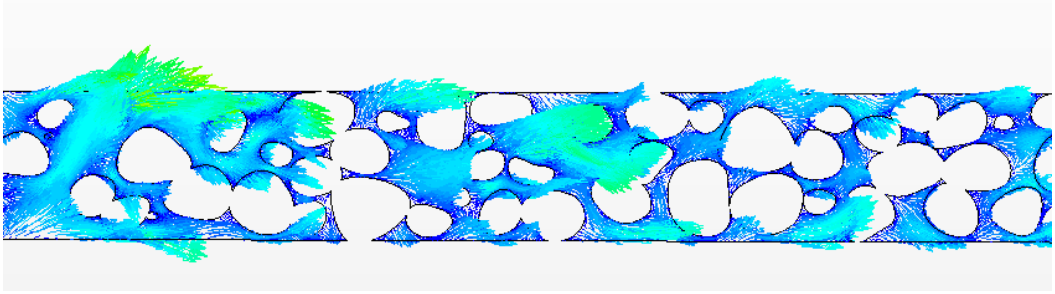

Figure 48: a) Axial locations at 2mm, 6mm, 10mm, 15mm, at a solution time of 2460s (41 mins) which show inlet effects, melt fronts. b) Vector plot of center sagittal slices that shows similar flow dynamics to that of Figure 42

Figure 48b shows a vector plot, which when compared with the quiver plot shown in Figure 42a shows similarities in the flow dynamics within the bed. In the sagittal and axial slices, maximum velocities in the range of 9mm/s to 10mm/s are seen which are slightly higher than those found in the previous models and in the experimental data. Once again, the reader is directed to ignore the maximum velocities shown in the center sagittal slice as it captures the inlet effects not seen in experimental data. This result of higher velocities begs the question as to why a faster melt front is not seen in this bed than that of the Spherical Gaussian model. At this time, the reason for this requires further analysis not presented in this thesis but speculations can be made and are presented later.

4.2.5 Discussion: NMR vs. CFD

The results obtained from the NMR experiment and three models are summarized in Table 5. As discussed in the previous sections all beds show similar maximum velocities in the range of 6 mm/s to 10 mm/s. In addition, similar preferential flow pathways and a similar pore structure are seen in the experimental bed, the Gaussian Spherical model and the Gaussian Non-Spherical model. Also, intra-particle melt and temperature gradients are seen in all packed beds.

Table 5: Summary of results from Experimental and Numerical Analysis of three beds.

Packed Bed	PCM Count	Melt Front Height (mm)	Maximum Velocity (mm/s)	Preferential Flow Pathways along the wall	Intra-Particle Gradients	Pore Structure Similarity w/ Experimental (Qualitative)
Experimental	178	60	7-8	✓	✓	
Constant Diameter	80	54	6-8	X	✓	X
Gaussian Spherical	170	18	6-7	✓	✓	✓
Gaussian Non-Spherical	173	13.5	9-10	✓	✓	✓

Various melt front heights, which is the bed melt height in 41 minutes were obtained for the experimental and CFD models. The experimental images yielded a melt front height of 60 mm in 41 minutes. In the CFD models, the bed with Monodisperse spheres showed a melt front height of 54 mm while the Spherical and Non-Spherical bed yielded a melt height of 18 mm and 13.5 mm, respectively, all within a time of 41 minutes. This shows that the Monodisperse spheres bed had the best comparison to the experimental data; however, as discussed previously, this bed had poor packing and a different pore structure to the experimental bed and so cannot be considered as a good complementary model.

This decision is further confirmed by the parameter defined as the PCM count. The PCM count is the physical number of PCMs that were packed in the respective

domains. As can be seen in Table 5, the Monodisperse bed model had almost 100 less PCMs than the experimental bed while the other two models contained a similar number of PCMs to the experimental bed. It can be deduced then, with current conditions, that the Monodisperse bed yielded an overly fast melt front.

Upon further examination into the Non-spherical model, a numerical error was seen in the progression of temperature and melt front. Figure 49a and Figure 49b shows a section of the melt front of this model at 2400s and 2460s, respectively. It can be seen that at 2400s the circled PCMs had completely melted and then at 2460s these PCM had solidified. This type of transition 'oscillation' was seen at various times and can cause a slower melt front than expected. The simulations were repeated two more times, one with a time step of 0.1s and the other with 40 maximum inner iterations to yield the same transition oscillation in both simulations.

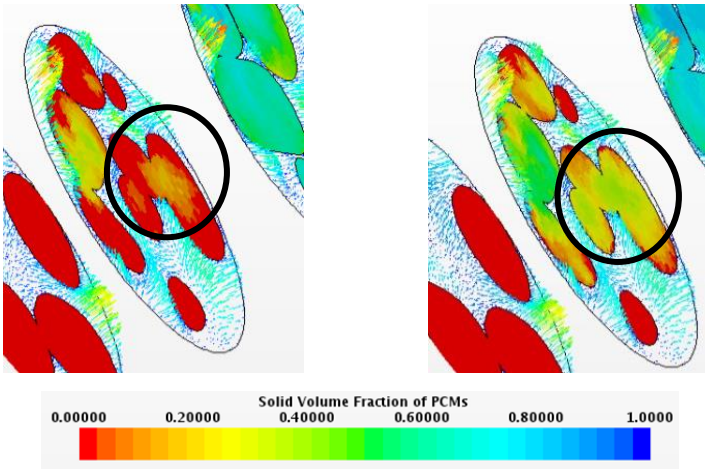

Figure 49: a) PCM melt fraction at 2400 showing almost a complete melt in PCM surfaces. b) PCM melt fraction at 2460s showing the same PCMs solidify.

Pure substances such as Eicosane melt at a single temperature, also known as the melting point and therefore, a sharp transition from solid to liquid phase exists. The PCM volumes in the CFD model were defined as pure Eicosane and a single melting point temperature of 310 K was specified. Star CCM+ applies an interval of 0.002 K to model

the melting and therefore changes the melting temperature range to occur from 309.999 K to 310.001 K. This interval is so small that it is still a sufficiently sharp transition from solid to liquid phase as shown by the blue line in Figure 50. This figure is a plot of enthalpy as a function of temperature. The area under the plot between the melt interval represents the latent heat of fusion. It must be noted that this plot is not drawn to scale and is shown here for a qualitative analysis.

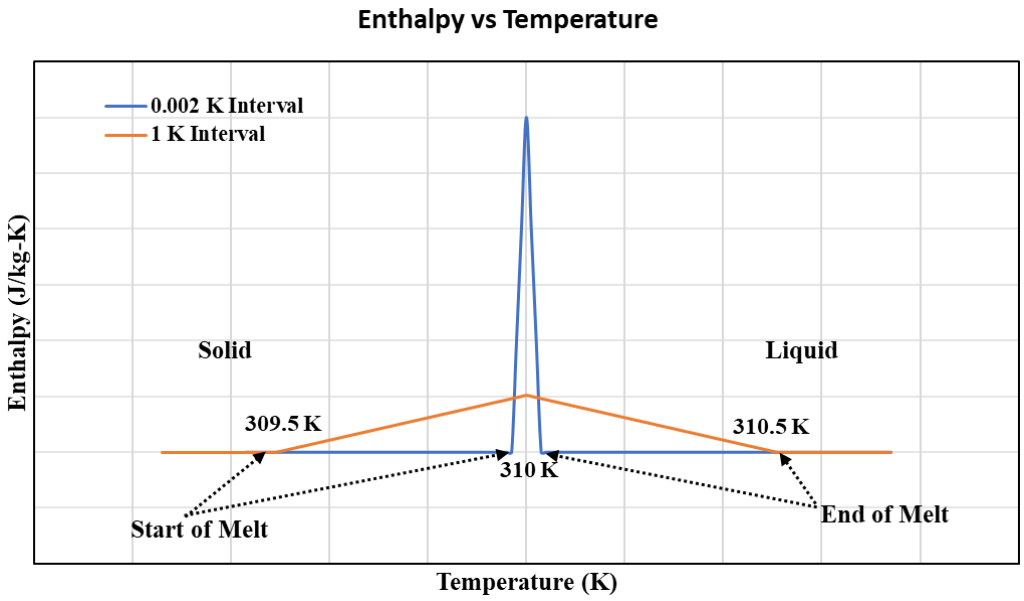

Figure 50: Enthalpy as a function of temperature for a substance. The area under the plot represents the Latent Heat of Fusion. The blue line represents a solid to liquid transition interval 0.002 K while the orange line represents a solid to liquid transition interval of 1 K.

Impure substances such as Glass melt over a range of temperatures with no sharp transition from solid to liquid phase. The PCM manufacturer has noted that the PCMs are impure substances and has specified that the melting temperature could range from 308 K to 312 K. Preliminary Differential Scanning Calorimetry (DSC) analysis of PCMs have also confirmed a larger transition interval than 0.002 K. The orange line in Figure 50 shows the transition from solid to liquid phase at a temperature interval of 1 K such that melting occurs at a temperature range between 309.5 K and 310.5 K. The latent heat of fusion must remain constant for both cases and so the areas under these lines must be the

same. Since the orange line has a larger interval, the peak of this line must be lower than the peak of the blue line in order to yield the same area and hence the same latent heat of fusion. The lower peak indicates that a smaller change in enthalpy per kelvin change within the melt transition is needed for a melt transition of 1 K than that of the 0.002 K melt transition. This infers that the 0.002 K interval specified in the models can significantly affect the melt front of the bed. This effect was explored by specifying an interval of 1 K such that the PCMs melt at a temperature range from 309.5 K to 310.5 K. Figure 51a and Figure 51b shows the final melt front of the 1 K interval and the 0.002 K interval, respectively. Figures 51a and 51b use a new color scale that shows more contrast in melting.

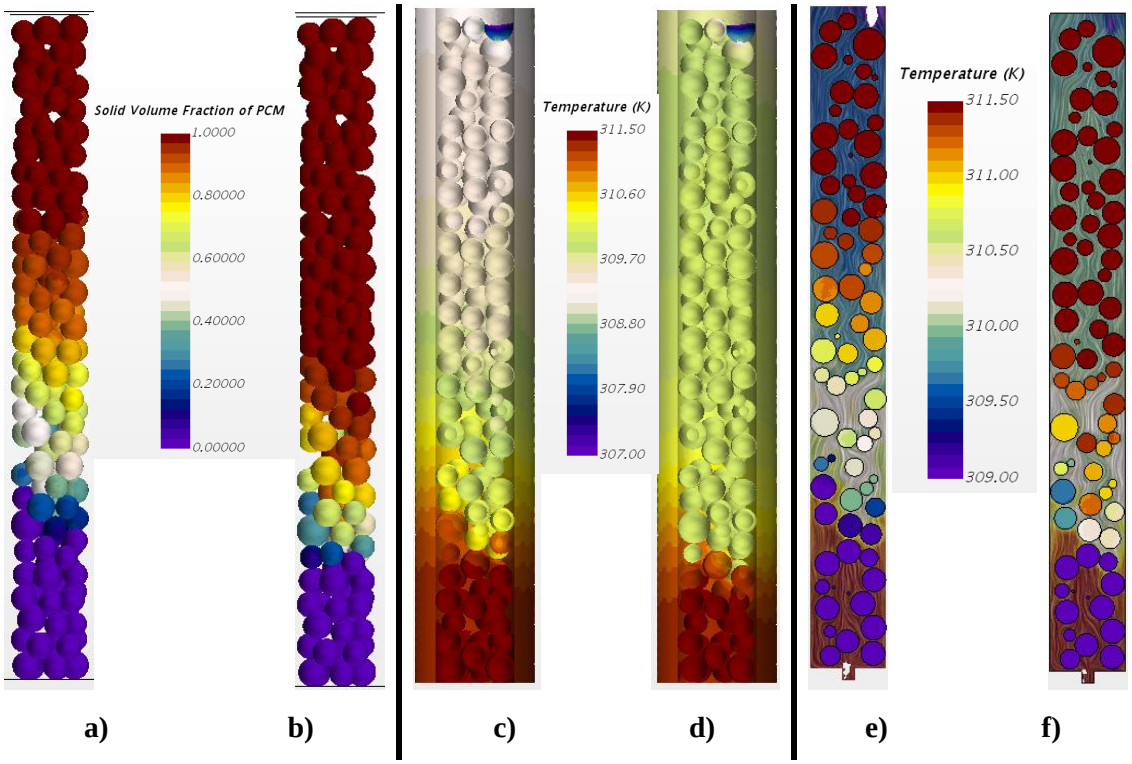

Figure 51: a) Melt front of 1 K interval model at a solution time of 2040s (34 mins). b) Melt front of 0.0 02 K interval model at a solution time of 2040s (34 mins). c) Temperature front of 1 K interval model at a solution time of 2040s (34 mins). d) Melt front of 0.002 K interval model at a solution time of 2040s (3 4 mins)

The 1 K interval model shows a faster melt front than the model with a 0.002 K interval. This indicates that the same amount of energy melted the same bed faster due to the larger interval. Figure 51c and Figure 51d shows the temperature front of the 1 K interval model and the 0.002 K interval model, respectively. The 1 K interval model shows a slower temperature front than that of the 0.002 K interval model. The melting PCMs act as energy sinks as thermal energy from the fluid is transferred into the PCMs for this phase transition. In the 1 K interval model, the PCMs act as energy sinks at a lower temperature causing the fluid to transfer energy at a lower temperature. In the 0.002 K interval model, the PCMs act as energy sinks at a higher temperature and so the energy transfer takes place at a higher temperature. Figure 51e and Figure 51f shows the temperature of the fluid for the 1 K interval model and the 0.002 K interval model, respectively. These figures show that the temperature of the fluid is lower higher up in the 1 K interval bed than that of the 0.002 K interval bed. Therefore, a slower temperature front is seen in the PCMs of the 1 K interval model.

5 CONCLUSIONS

The work presented in this thesis shows experimental data of flow and heat transfer in a packed bed that is then modelled in a CFD application using experimental conditions. Experiments done in previous literature utilize invasive techniques such as thermocouple probes to obtain pore scale information, which can affect the flow dynamics of the bed. However, NMR imaging is a non-invasive technique that avoids this issue. The NMR results presented captured melt fronts and melt fractions in a packed bed of PCMs and mapped the velocities of the fluid. 2D intensity images captured using ^{1}H imaging show clearly visible melt fronts, pore structures and intra-particles melt gradients at high spatial resolutions.

Initially, the melting of PCMs was achieved by flowing heated Nitrogen through the packed bed. The results obtained from this experiment indicated preferential flow pathways through faster melting of PCMs at certain regions. In addition, intra-particle melt gradients were clearly seen in these images, which shows the sufficient high spatial resolution achieved from NMR imaging. The numerical model showed a melt height of 75 mm in 57 minutes while the experimental work yielded a melt height of 50 mm in 57 minutes. The inlet mass flow rate of the numerical model was calculated using the density of Nitrogen at standard temperature and pressure while the actual density of Nitrogen in experimental work is much lower. This resulted in a faster mass flow rate than in experimental work and is suspected to be the reason for the faster melt front. The numerical models also showed indications of preferential flow pathways as well while also showing intra-particle melt gradient in the sagittal slices captured. However, velocity maps obtained from the numerical model could not be verified with experimental work due to NMR equipment not being able to image Nitrogen flow.

Therefore, further experiments were conducted where PCMs were melted by flowing heated Fluorinert through the packed bed. This enabled the coupling of melt fronts with velocity maps using ^{19}F imaging to yield information regarding the flow of the liquid phase through the pore structure, including the preferential flow pathways along the wall discussed in literature [8, 9, 18, 19]. This work is fundamental in future

work that will enable the coupling of temperature, heat transfer and velocity maps at the pore scale that can help better understand the physics behind packed beds. These experimental conditions were used to inform complementary numerical models so that numerical results can be compared with experimental results. Once a numerical model can be successfully validated by NMR experimental work, this can help develop models for larger applications that utilize flow and heat transfer in packed beds such as thermal energy storage, and catalytic reactors.

In the development of the bed, the first challenge was the generation of a bed of similar pore structure to that of the experimental bed. In doing this, three models were developed: a packed bed of monodisperse spheres, Spherical particles with a Gaussian distribution in diameters and Non-Spherical particles with a Gaussian distribution in diameters. Using the parameters shown in Table 5, it was determined that the Gaussian Spherical and the Gaussian Non-Spherical bed models were the best complementary models to the experimental work. More specifically, the PCM count, maximum velocities yielded, melt front heights and flow characteristics through the pore structure were the conclusive factors for this decision. Although the melt front height of the Constant Diameter bed (=54 mm) showed the closest result to that of the experimental work (=60 mm), it was determined that this bed had poor packing causing an overly fast melt front at the current CFD conditions. It is believed that this determination will be more clearly demonstrated once the model conditions are further perfected using the recommendations suggested in the next section.

It was also concluded that the modelling of the PCMs as pure Eicosane has a significant effect on the heat transfer processes. Experimental PCMs contained impurities that results in a larger melt transition than the sharp transition of 0.002 K modelled in numerical work. Preliminary DSC analysis of experimental PCMs has confirmed a larger transition interval. A CFD model was built with PCMs having a 1 K transition interval yielding a faster melt front than seen with the 0.002 K interval model.

6 RECOMMENDATIONS

As discussed in the previous sections, it is believed that these models and experimental work can be improved to better complement each other. One issue with experimental work was determining accurate inlet conditions, more specifically, Fluorinert inlet temperature. Although a well-insulated heat exchange system was used to transport Fluorinert from the pump to the NMR equipment, there is considerable heat loss during the transport from the pump and the actual inlet temperature is less than the temperature the Fluorinert was heated to initially. For instance, the heat bath was set to 75.5 °C while the inlet temperature of the Fluorinert was determined to be at 38.5 °C. This inlet measurement was done by inserting a thermocouple into the tube at the inlet such that it would be parallel to the flow of Fluorinert. It is believed that the thermocouple could have actually touched the walls of the transporting tube resulting in an inaccurate temperature reading. This inaccuracy is further confirmed by the inlet temperatures recorded that showed considerable oscillation in readings over time. It is recommended that a rigid thermocouple should be connected perpendicular to the flow as shown in Figure 52, such that the thermocouple does not touch the walls of the tube.

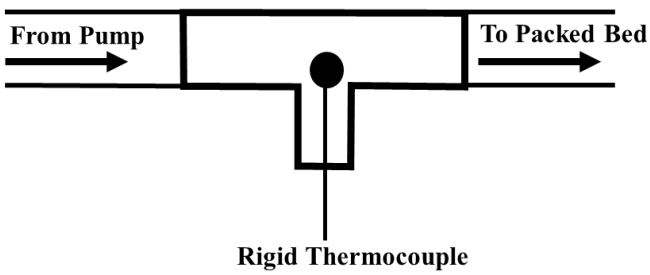

Figure 52: Schematic for more accurate measurement of inlet temperatures. Temperature sensor placed perpendicular to the flow.

In order to better the CFD models several improvements are recommended. In experiments, encapsulated PCMs acquired from Microtek laboratories were utilized where Eicosane is encapsulated with a propriety polymer. Although the manufacturer states that roughly 80% of the PCM is Eicosane, the models assumed that 100% of the

volume is Eicosane. This difference in mass that can melt can significantly affect the rate of heat transfer and the total energy needed to melt the PCMs. One method proposed is to use 80% of the latent heat of fusion value used currently as this would yield the same result from the energy equation if the 80% of the mass was used.

Furthermore, it is believed that the effective heat capacity and latent heat of fusion of the PCMs are different than those used in the models shown in Table 3, which were obtained for pure Eicosane from the manufacturer. Due to the proprietary nature of the encapsulation used, accurate values cannot be calculated. Therefore, preliminary Differential Scanning Calorimetry (DSC) experiments on PCMs have been conducted that have yielded values that are approximately 33% different from the heat capacity and latent heat of fusion values used in the models. Once accurate and conclusive DSC data is received, values used in models should be changed to better complement the experimental work.

In addition, the outer wall heat transfer coefficient was defined as 0.5 W/m^2-K which was an educated guess. A more accurate heat transfer coefficient can be calculated experimentally to ensure an accurate modelling of the outer-wall heat loss. A method is proposed where local temperatures on the outer wall of the packed bed can be determined by utilizing multiple thermocouples. By using the temperature values obtained, an average heat transfer coefficient can be calculated that can better inform the model.

The figures on Star CCM+ were saved every 60 seconds, which allowed for a sufficiently high temporal resolution of the melt and temperature front progression to be captured. For a better capture of the intra-particle melt gradients of the PCMs, this frequency should be increased such that an image is captured every

The PCMs in the CFD models were to set to melt in a temperature interval of 0.002 K. However, preliminary DSC analysis have found that these PCMs melt in a range of temperatures due to other impurities in the PCMs such as the proprietary polymer shell. Preliminary analysis of a model that contained PCMs with a 1 K transition interval was found to cause a significantly faster melt front. Therefore, it is recommended that the melting temperatures of the PCMs specified in the CFD model be changed to reflect the actual melting temperature range.

REFERENCES CITED

1. Nield, D.A., A. Bejan, and Nield-Bejan, *Convection in porous media*. Vol. 3. 2006: Springer.

2. Mills, P. and R. Chaudhari, *Multiphase catalytic reactor engineering and design for pharmaceuticals and fine chemicals.* Catalysis Today, 1997. **37**(4): p. 367-404.

3. Groppi, G. and E. Tronconi, *Simulation of structured catalytic reactors with enhanced thermal conductivity for selective oxidation reactions.* Catalysis Today, 2001. **69**(1): p. 63-73.

4. Kuravi, S., et al., *Thermal energy storage technologies and systems for concentrating solar power plants.* Progress in Energy and Combustion Science, 2013. **39**(4): p. 285-319.

5. Wildenschild, D. and A.P. Sheppard, *X-ray imaging and analysis techniques for quantifying pore-scale structure and processes in subsurface porous medium systems.* Advances in Water Resources, 2013. **51**: p. 217-246.

6. Blunt, M.J., et al., *Pore-scale imaging and modelling.* Advances in Water Resources, 2013. **51**: p. 197-216.

7. Ergun, S., *Fluid Flow Through Packed Columns.* Chemical Engineering Progress, 1952. **Volume 48**: p. 89-94.

8. Cheng, N.-S., *Wall effect on pressure drop in packed beds.* Powder Technology, 2011. **210**(3): p. 261-266.

9. Di Felice, R. and L. Gibilaro, *Wall effects for the pressure drop in fixed beds.* Chemical engineering science, 2004. **59**(14): p. 3037-3040.

10. Macdonald, I., et al., *Flow through porous media-the Ergun equation revisited.* Industrial & Engineering Chemistry Fundamentals, 1979. **18**(3): p. 199-208.

11. Eisfeld, B. and K. Schnitzlein, *The influence of confining walls on the pressure drop in packed beds.* Chemical Engineering Science, 2001. **56**(14): p. 4321-4329.

12. Hsu, C. and P. Cheng, *Thermal dispersion in a porous medium.* International Journal of Heat and Mass Transfer, 1990. **33**(8): p. 1587-1597.

13. Hsu, C. and P. Cheng, *Closure schemes of the macroscopic energy equation for convective heat transfer in porous media.* International communications in heat and mass transfer, 1988. **15**(5): p. 689-703.

14. Hsu, C., *A closure model for transient heat conduction in porous media.* TRANSACTIONS-AMERICAN SOCIETY OF MECHANICAL ENGINEERS JOURNAL OF HEAT TRANSFER, 1999. **121**: p. 733-738.

15. Whitaker, S., *Flow in porous media I: A theoretical derivation of Darcy's law.* Transport in porous media, 1986. **1**(1): p. 3-25.

16. Pfitzner, J., *Poiseuille and his law.* Anaesthesia, 1976. **31**(2): p. 273-275.

17. Vafai, K., *Convective flow and heat transfer in variable-porosity media.* Journal of Fluid Mechanics, 1984. **147**: p. 233-259.

18. Mehta, D. and M. Hawley, *Wall effect in packed columns.* Industrial & Engineering Chemistry Process Design and Development, 1969. **8**(2): p. 280-282.

19. Foumeny, E., et al., *Correlations of pressure drop in packed beds taking into account the effect of confining wall.* International journal of heat and mass transfer, 1993. **36**(2): p. 536-540.

20. McGreavy, C., E. Foumeny, and K. Javed, *Characterization of transport properties for fixed bed in terms of local bed structure and flow distribution.* Chemical Engineering Science, 1986. **41**(4): p. 787-797.

21. Blake, F., *The resistance of packing to fluid flow.* Transactions of the American Institute of Chemical Engineers, 1922. **14**(415-421): p. 3.

22. Nemec, D. and J. Levec, *Flow through packed bed reactors: 1. Single-phase flow.* Chemical Engineering Science, 2005. **60**(24): p. 6947-6957.

23. Sonntag, G., *Einfluß des Lückenvolumens auf den Druckverlust in gasdurchströmten Füllkörpersäulen.* Chemie Ingenieur Technik, 1960. **32**(5): p. 317-329.

24. Hilton, J., L. Mason, and P. Cleary, *Dynamics of gas–solid fluidised beds with non-spherical particle geometry.* Chemical Engineering Science, 2010. **65**(5): p. 1584-1596.

25. Wadell, H., *Volume, shape, and roundness of quartz particles.* The Journal of Geology, 1935. **43**(3): p. 250-280.

26. Colburn, A.P., *Heat transfer and pressure drop in empty, baffled, and packed tubes1.* Industrial & Engineering Chemistry, 1931. **23**(8): p. 910-913.

27. Cheng, P., A. Chowdhury, and C. Hsu, *Forced convection in packed tubes and channels with variable porosity and thermal dispersion effects,* in *Convective heat and mass transfer in porous media*. 1991, Springer. p. 625-653.

28. Nozad, I., R. Carbonell, and S. Whitaker, *Heat conduction in multiphase systems—I: theory and experiment for two-phase systems.* Chemical Engineering Science, 1985. **40**(5): p. 843-855.

29. Zehner, P. and E. Schlünder, *Wärmeleitfähigkeit von Schüttungen bei mäßigen Temperaturen.* Chemie Ingenieur Technik, 1970. **42**(14): p. 933-941.

30. Hsu, C., P. Cheng, and K. Wong, *Modified Zehner-Schlunder models for stagnant thermal conductivity of porous media.* International journal of heat and mass transfer, 1994. **37**(17): p. 2751-2759.

31. Tsotsas, E. and H. Martin, *Thermal conductivity of packed beds: a review.* Chemical Engineering and Processing: Process Intensification, 1987. **22**(1): p. 19-37.

32. Ofuchi, K. and D. Kunii, *Heat-transfer characteristics of packed beds with stagnant fluids.* International Journal of Heat and Mass Transfer, 1965. **8**(5): p. 749-757.

33. Cundall, P.A. and O.D. Strack, *A discrete numerical model for granular assemblies.* geotechnique, 1979. **29**(1): p. 47-65.

34. Fatt, I., *The network model of porous media.* 1956.

35. Chareyre, B., et al., *Pore-scale modeling of viscous flow and induced forces in dense sphere packings.* Transport in porous media, 2012. **94**(2): p. 595-615.

36. Catalano, E., B. Chareyre, and E. Barthélemy, *Pore-scale modeling of fluid-particles interaction and emerging poromechanical effects.* International Journal for Numerical and Analytical Methods in Geomechanics, 2014. **38**(1): p. 51-71.

37. Rong, L., K. Dong, and A. Yu, *Lattice-Boltzmann simulation of fluid flow through packed beds of uniform spheres: Effect of porosity.* Chemical Engineering Science, 2013. **99**: p. 44-58.

38. Dalman, M., J. Merkin, and C. McGreavy, *Fluid flow and heat transfer past two spheres in a cylindrical tube.* Computers & fluids, 1986. **14**(3): p. 267-281.

39. Nijemeisland, M. and A.G. Dixon, *CFD study of fluid flow and wall heat transfer in a fixed bed of spheres.* AIChE Journal, 2004. **50**(5): p. 906-921.

40. Thompson, K.E. and H.S. Fogler, *Modeling flow in disordered packed beds from pore-scale fluid mechanics.* AIChE Journal, 1997. **43**(6): p. 1377-1389.

41. Visscher, W.M. and M. Bolsterli, *Random packing of equal and unequal spheres in two and three dimensions.* Nature, 1972. **239**(5374): p. 504-507.

42. Eppinger, T., K. Seidler, and M. Kraume, *DEM-CFD simulations of fixed bed reactors with small tube to particle diameter ratios.* Chemical Engineering Journal, 2011. **166**(1): p. 324-331.

43. Kawaguchi, T., T. Tanaka, and Y. Tsuji, *Numerical simulation of two-dimensional fluidized beds using the discrete element method (comparison between the two-and three-dimensional models).* Powder technology, 1998. **96**(2): p. 129-138.

44. Tanaka, T., T. Kawaguchi, and Y. Tsuji, *Discrete particle simulation of flow patterns in two-dimensional gas fluidized beds.* International Journal of Modern Physics B, 1993. **7**(09n10): p. 1889-1898.

45. Tsuji, Y., T. Kawaguchi, and T. Tanaka, *Discrete particle simulation of two-dimensional fluidized bed.* Powder technology, 1993. **77**(1): p. 79-87.

46. Bai, H., et al., *A coupled DEM and CFD simulation of flow field and pressure drop in fixed bed reactor with randomly packed catalyst particles.* Industrial & Engineering Chemistry Research, 2009. **48**(8): p. 4060-4074.

47. Ookawara, S., et al. *High-fidelity DEM-CFD modeling of packed bed reactors for process intensification*. in *Proceedings of European Congress of Chemical Engineering (ECCE-6), Copenhagen*. 2007.

48. Li, C.-H. and B.A. Finlayson, *Heat transfer in packed beds—a reevaluation.* Chemical Engineering Science, 1977. **32**(9): p. 1055-1066.

49. De Wasch, A. and G. Froment, *Heat transfer in packed beds.* Chemical Engineering Science, 1972. **27**(3): p. 567-576.

50. Nesbitt, G., et al., *Towards validation of porous media models using NMR imaging and image-analysis techniques.* Magnetic resonance imaging, 1991. **9**(5): p. 779-787.

51. Sederman, A., et al., *Magnetic resonance imaging of liquid flow and pore structure within packed beds.* Chemical Engineering Science, 1997. **52**(14): p. 2239-2250.

52. Seymour, J.D. and P.T. Callaghan, *Generalized approach to NMR analysis of flow and dispersion in porous media.* AIChE Journal, 1997. **43**(8): p. 2096-2111.

53. Yang, X., et al., *Direct numerical simulation of pore-scale flow in a bead pack: Comparison with magnetic resonance imaging observations.* Advances in Water Resources, 2013. **54**: p. 228-241.

54. Bloembergen, N., E.M. Purcell, and R.V. Pound, *Relaxation effects in nuclear magnetic resonance absorption.* Physical review, 1948. **73**(7): p. 679.

55. Parker, D.L., et al., *Temperature distribution measurements in two-dimensional NMR imaging.* Medical physics, 1983. **10**(3): p. 321-325.

56. Quesson, B., J.A. de Zwart, and C.T. Moonen, *Magnetic resonance temperature imaging for guidance of thermotherapy.* Journal of Magnetic Resonance Imaging, 2000. **12**(4): p. 525-533.

57. Jarenwattananon, N.N., et al., *Thermal maps of gases in heterogeneous reactions.* arXiv preprint arXiv:1506.06334, 2015.

58. Callaghan, P.T., *Translational dynamics and magnetic resonance: principles of pulsed gradient spin echo NMR*. 2011: Oxford University Press.

59. Torrey, H.C., *Bloch equations with diffusion terms.* Physical review, 1956. **104**(3): p. 563.

60. Automation Creations, I. *MatWeb*. 2011; Available from: http://www.matweb.com/search/search.aspx.

61. Reprinted from Chemical Engineering Science, Vol 41, No. 4, C. McGreavy, E.A. Foumeny, K.H Javed, C*harcterization of Transport Properties for Fixed Bed in terms of Local Bed Structure and Flow Distribution*, Pg 787-797, Copyright 1986, with permission from Elsevier

APPENDICES

APPENDIX A

STRESS ANALYSIS OF PEEK SAMPLE HOLDER

STRESS ANALYSIS ON SAMPLE HOLDER

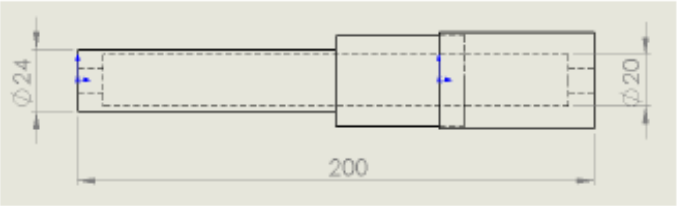

Assumptions:
1. Thin Walled Pressure Vessel
2. Static Pressure

$r_o := 12.5\ mm$ <---- maximum outer radius possible

$\sigma_{yield} := 75\ MPa$ <---- yield stress of PEEK

σ_{max} <---- maximum stress on sample holder

$SF = \frac{\sigma_{yield}}{\sigma_{max}}$ <----- Safety Factor

$\frac{\sigma_{yield}}{\sigma_{max}} \geq 1.5$ (1) <----- Safety Factor of 1.5 used for design

$\sigma_y = \frac{P_{max} r_i}{t}$ $\sigma_x = \frac{P_{max} r_i}{2\ t}$ $\sigma_y > \sigma_x$ $\sigma_y = \sigma_{max}$ <---- Maximum stress in sample holder

$P_{max} := 100\ bar$ <---- Maximum Pressure in sample holder

$t = r_o - r_i$ <---- thickness of sample holder

r_i <----- inner radius of sample holder

solved (1) for inner radius

$$r_i := \frac{r_o}{\frac{1.5 \cdot P_{max}}{\sigma_{yield}} + 1} = 10.417\ mm$$ <----- maximum inner radius

Inner radius of 10 mm used for design

APPENDIX B

EXPERIMENTAL ISSUES

Experimental Issues

The initial Fluorinert flow loop pumped pre-heated Fluorinert that sat in a heat bath. The heated Fluorinert caused the O-rings in the HPLC pump to melt, which was then pumped into the bed together with the Fluorinert. This caused O-ring residue to settle in the packed bed changing the physical pore structure of the bed. This O-ring residue also caused blockages in the HPLC tubes used to transport Fluorinert, which resulted in an increase in pressure in the system. This was fixed by changing the flow loop to the aforementioned loop where the Fluorinert is heated after the pump so that the pump does not experience high temperatures.

Another issue that had to be dealt with was heat loss in the Fluorinert as it was transported from the pump to the packed bed. It was determined that the Fluorinert would lose as much as 70 °C between the pump and the packed bed. Therefore, the heat exchanger system shown in Figure 15b was used to minimize the heat loss. Hot water was passed alongside the Fluorinert transporting tubes, which were both insulated with 1/2”Armaflex pipe insulation.

Custom made fittings were necessary to connect the tubes to the packed beds. This is because fittings made out of PEEK material was necessary to ensure the NMR signals were not affected during imaging. NPT/Compression Fittings were necessary to connect the HPLC tube to the packed bed. These fittings were custom made by Valco Instruments and used in the packed bed used in the Nitrogen experiment. These fittings however had a relatively low fatigue life compared to stainless steel fittings. Since these fittings experienced relatively high pressure and temperatures, these fittings started to crack and cause leaks after a number of uses.

APPENDIX C

CFD ISSUES

CFD Issues

Initially, the heat transfer and flow were analyzed using the DEM method where the bed was filled with DEM particles that changed in temperature as the fluid was flowed through the bed. However, this method of using the DEM cause the fluidization of the bed, which was not seen in the experimental bed. This method also demands high computational cost, which meant that the CFD models ran very slowly. Furthermore, a simple method was not available to model the melting of DEM particles. Due to these reasons, the DEM method was only used to generate a randomly packed bed. Even without the use of DEM, the CFD models still required a lot of computational resources. The file sizes of a completely run model were as large as 2GB. It was determined that it would take a week to a run a solution time of 34 minutes on a single Core i7-2600 3.40 GHz processor with a RAM of 8 GB. This issue was rectified by uploading the simulation to a computing cluster that brought the simulation run time to approximately 15 hours.

For the generation of the non-spherical bed, three frequently occurring shapes in the experimental PCMs were modelled on Star CCM+. These non-spherical particles contained flat surfaces that made contact with other particle during packing. These contact areas caused surface meshing issues. The various curvatures at points of contact was not meshed successfully causing low surface qualities during meshing as seen in Figure 53.

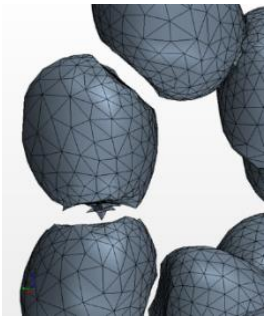

Figure 53: Surface meshing of non-spherical particles caused low surface qualities at points of contact between non-spherical particles

It was decided that these points of contact would be joined together by uniting these surfaces. This resulted in PCMs in contact with the wall and each other to be modelled as one body. In addition, a continuum based mesh was used instead of a part based mesh that was used for the other models. This yielded a successful surface mesh that did not alter the PCM surface.

APPENDIX D

ADIABATIC VS. NON-ADIABATIC WALLS

Adiabatic vs Non-Adiabatic Walls

The models discussed in the previous sections had non-adiabatic walls with the same wall thickness as the cylinder used in the experimental data. The outer wall was set as a convective heat loss boundary to an ambient temperature of 22 °C as in the laboratory. The heat transfer coefficient was set to 0.5 W/m^2-K. A bed with adiabatic walls was also modelled as seen in Figure 54a. Consistent with theory, this bed shows a faster temperature front than that of the non-adiabatic bed seen in Figure 54b.

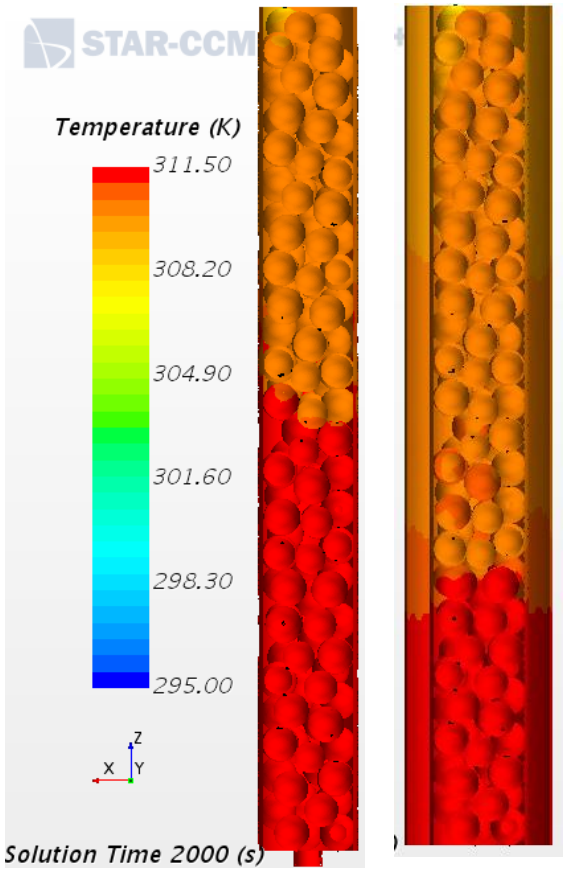

(a) **(b)**

Figure 54: a) Temperature front through a bed with adiabatic walls b) Temperature front through a bed with non-adiabatic walls showing a slower temperature front than a) due to wall heat losses.